EUROPEAN ORGANISATION FOR NUCLEAR RESEARCH

CERN-EP/2004-XXX
14 July 2004

Measurement of the running of the QED coupling in small angle Bhabha scattering at LEP

OPAL Collaboration

Abstract

Using the OPAL detector at LEP, the running of the effective QED coupling $\alpha(t)$ is measured for space-like momentum transfer $1.8 \leq -t \leq 6.0$ GeV^2 through its effect on the angular spectrum of small angle Bhabha scattering. In an almost ideal QED framework, with very favourable experimental conditions, we obtain the strongest direct evidence ever presented that the running of α is consistent with Standard Model expectations. The null hypothesis that α remains constant within the above interval of $-t$ is excluded with a significance above 5 σ. Similarly, our results are inconsistent at the level of about 3 σ with the hypothesis that only leptonic loops contribute to the running, and therefore provide the first clear experimental evidence that hadronic loops also contribute.

Authors:
G. Abbiendi, P. Guenther, M. Kobel

Please send comments by Wednesday 28th July 2004 to:
abbiendi@bo.infn.it, guenther@physik.uni-bonn.de, mkobel@physik.uni-bonn.de

1 Introduction

The electromagnetic coupling constant is a basic parameter of the Standard Model, known with a relative precision of 4×10^{-9} [1] at zero momentum transfer. In QED the effective coupling changes, or *runs*, with the scale of momentum transfer due to vacuum polarization. This is due to virtual lepton or quark loop corrections to the photon propagator. This effect can also be understood as an increasing penetration of the polarized cloud of virtual particles which screen the bare electric charge of a particle as it is probed at smaller and smaller distance. The effective QED coupling is generally expressed as:

$$\alpha(Q^2) = \frac{\alpha_0}{1 - \Delta\alpha(Q^2)} \tag{1}$$

where $\alpha_0 = \alpha(Q^2 = 0) \simeq 1/137.036$ is the fine structure constant.

The value of $\Delta\alpha$ can be calculated in field theory. Whereas the leptonic contributions are calculable to very high accuracy, the hadronic ones are more problematic as they involve quark masses and hadronic physics at low momentum scales. The hadronic contribution can be most precisely determined through its relation to a dispersion integral over a parameterization of the measured annihilation cross section of $e^+e^- \rightarrow$ *hadrons*, supplemented with perturbative QCD above resonances [2, 3]. The main difficulty of this approach comes from the integration of experimental data in the region of hadronic resonances, which in turn gives the dominant uncertainty on $\Delta\alpha$ for positive (*time-like*) Q^2. The effective QED coupling $\alpha(Q^2)$ is an essential ingredient for many precision physics predictions. It contributes one of the dominant uncertainties in the electroweak fits constraining the Higgs mass [4]. There are also many evaluations which are more theory-driven, extending the application of perturbative QCD down to about 2 GeV (see for example the references in [4]). An alternative approach uses the Adler function [5] and perturbative QCD in the negative Q^2 (*space-like*) region [6], where $\Delta\alpha$ is a smooth function.

Until now there have been only a few direct observations of the running of the QED coupling [7, 8, 9, 10]. Most of these analyses involve measurements of cross sections and their ratios and obtain values of $\alpha(Q^2)$ which are found to deviate from α_0 or from the assumed value of the coupling at some initial scale. Theoretical uncertainties on the predicted absolute cross sections as well as experimental scale errors can influence such determinations or reduce their significance. The s-channel results from the TOPAZ [7] and the OPAL [8] experiments were based on e^+e^-annihilations to leptonic final states. Far enough from the Z resonance these processes are dominated by single photon exchange, although they substantially involve the full electroweak theory. Large angle Bhabha scattering has been studied by the VENUS [9] and L3 [10] experiments to measure the running in the space-like region. In this case both s- and t-channel γ-exchange diagrams are important and the effective QED coupling appears as a function of s or t respectively. Moreover interference contributions due to Z exchange are also sizeable.

In this paper we measure the running of α in the space-like region, by studying the angular dependence of small angle Bhabha scattering. The square of the momentum transfer t is simply related to the polar scattering angle, and the scattering spectrum is modified by the running coupling which appears as $\alpha^2(t)$. We use the small angular region accepted for the luminosity measurement, which approximately corresponds to $2 \leq -t \leq 6$ GeV^2 at centre-of-mass energy

near the Z resonance peak. At this t scale the average $\Delta\alpha$ is about 2%. The number of small angle Bhabha events is used to determine the integrated luminosity, so that we will not make an absolute measurement of $\alpha(t)$, rather we will look only at the variation of $\Delta\alpha$ across the acceptance, which is expected to be about 0.5%, leading to an observable effect of about 1%. An interesting property of this low $|t|$ region is that, although the absolute $\Delta\alpha$ value is dominated by the leptonic contributions, the leptonic and hadronic components contribute about equally to its variation across the region accessible to our measurements. There has been only one similar attempt [10] to test the momentum transfer dependence of α directly in a way free of normalization errors. There exists no previous direct experimental evidence for the hadronic contribution to the running.

Small angle Bhabha scattering appears to be an ideal process for a direct measurement of the running of $\alpha(Q^2)$ in a single experiment. Among the advantages are the high available statistics and the purity of the data sample. In this work a crucial element has been the very high precision in measuring the scattering angle provided by the OPAL Silicon-Tungsten (SiW) luminometer [12]. Not less important is the cleanliness of the measurement from a theoretical point of view, which has also been pointed out recently [11]. Small angle Bhabha scattering is strongly dominated by single-photon t-channel exchange, while s-channel photon exchange is practically negligible. It is currently exactly calculable up to the leading $\mathcal{O}(\alpha^2)$ terms in the QED photonic corrections (herein indicated as $\mathcal{O}(\alpha^2 L^2)$, where $L = \ln(|t|/m_e^2) - 1$ is the large logarithm). Many existing calculations are described in [13] and were also widely cross-checked, mainly to reduce the theoretical error on the determination of the luminosity at LEP1. Higher order terms are partially accounted for through exponentiation. Many of these calculations are available in the convenient form of Monte Carlo programs which also have been extensively checked by the LEP experiments. A calculation accurate to the subleading $\mathcal{O}(\alpha^2)$ terms [14] also exists. Corrections for Z interference are very small and well known, so that small angle Bhabha scattering near the Z pole can be considered an essentially pure QED process. A comparison of data with such precise calculations can determine the value of the effective QED coupling in the most accurate way without relying on the correctness of the SU(2)×U(1) electroweak model.

The paper is organized as follows: We explain the analysis method in section 2, the detector and its Monte Carlo simulation is briefly described in section 3 and the event selection in section 4. The procedure to correct the data distributions is explained in section 5. The fit results including only statistical errors are given in section 6, while the systematic errors are described in detail in section 7. The theoretical uncertainties are discussed in section 8. The results are finally given in section 9, and a conclusive summary in section 10.

2 Analysis method

The Bhabha differential cross section can be written in the following form for small scattering angle:

$$\frac{\mathrm{d}\sigma}{\mathrm{dt}} = \frac{\mathrm{d}\sigma^{(0)}}{\mathrm{dt}} \left(\frac{\alpha(t)}{\alpha_0} \right)^2 (1+\epsilon)\ (1+\delta_\gamma) + \delta_Z \tag{2}$$

where:

$$\frac{\mathrm{d}\sigma^{(0)}}{\mathrm{dt}} = \frac{4\pi\alpha_0^2}{t^2} \tag{3}$$

is the Born term for t-channel single photon exchange, α_0 is the fine structure constant and $\alpha(t)$ is the effective coupling at the momentum transfer scale t. Here ϵ represents the radiative corrections to the Born cross section, δ_γ the contribution of s-channel photon exchange and δ_Z the contribution of Z exchange, mostly from interference. The contributions of δ_γ and δ_Z are much smaller than those of ϵ and the vacuum polarization. Therefore with a precise knowledge of the radiative corrections (ϵ term) one can determine the effective coupling $\alpha(t)$ by measuring the differential cross section. The form of equation (2) is an approximation since the δ_γ term is not really factorizable with the effective coupling $\alpha^2(t)$. In fact the s-channel amplitude couples as $\alpha(s)$. The practical validity of equation (2) is a consequence of the smallness of the δ_γ term, which could even be neglected.

The counting rate of Bhabha events in the SiW luminometers is used to determine the integrated luminosity, so that we cannot make an absolute measurement of $\alpha(t)$, without an independent determination of the luminosity. Instead, the structure of the cross section as written in (2) easily allows the variation of $\alpha(t)$ over the accessible t range to be determined, since the dominant piece of the cross section contains the factor $(\alpha(t)/\alpha_0)^2$. At leading order the variable t is simply related to the scattering angle:

$$t = -s\,\frac{1-\cos\theta}{2} \approx -\frac{s\,\theta^2}{4} \tag{4}$$

Photon radiation (in particular initial-state radiation) smears this correspondence. The event selection that we use, described in section 4, has been carefully studied to reduce the impact of radiative events. In particular the energy cuts and the acollinearity cut are very effective. As a result the event sample is strongly dominated by two-cluster configurations, with almost full energy back-to-back scattered e^+ and e^-. For such a selection the relation (4) represents a good approximation. The polar scattering angle θ is measured from the radial position R of the scattered e^+ and e^- at reference planes located within the SiW luminometers, at a distance z from the interaction point:

$$\theta = \arctan(R/z) \tag{5}$$

We use the BHLUMI [15] Monte Carlo generator for all calculations of small angle Bhabha scattering. It is a multiphoton exponentiated generator accurate up to the leading logarithmic $\mathcal{O}(\alpha^2)$ terms. Higher order photonic contributions are partially included by virtue of the exponentiation. The generated events always contain the scattered electron and positron plus an arbitrary number of (non-collinear) photons. Small contributions from s-channel photon exchange and Z interference are also included. Corrections due to vacuum polarization are implemented with a few choices for the parameterization of the hadronic term [2, 16]. We used the option to generate weighted events, such that we could access all the available intermediate weights which compose the final complete cross section event by event. In particular we could also modify the parameterization of the vacuum polarization or set $\alpha(t) \equiv \alpha_0$ to assume a fixed coupling α_0.

We will compare the radial distribution of the data (and hence the t-spectrum) with the predictions of the BHLUMI Monte Carlo to determine the running of α within the accepted region.

We calculated the ratios of data and Monte Carlo events in each bin. If the Monte Carlo is modified by setting the coupling to the constant value $\alpha(t) \equiv \alpha_0$, then:

$$R(t) = \frac{N_{data}}{N^0_{MC}} \propto \left(\frac{1}{1 - \Delta\alpha(t)} \right)^2 . \tag{6}$$

The dominant dependence of $\Delta\alpha(t)$ expected from theory is logarithmic. However, within the kinematic region of this analysis and the statistical sensitivity of the data, the expected dependence may be approximated with a straight line. We fitted the ratios as:

$$R(t) = a + b\,|t| \,. \tag{7}$$

The value of t in each bin is calculated according to Equation 4, averaged over the bin, assuming the cross section dependence of Equation 3. The errors associated with these approximations are negligable, and discussed in Section 7.9. The slope b represents the full observable effect of the running of $\alpha(t)$, both the leptonic and hadronic components. It is related to the variation of the coupling by:

$$\Delta\alpha(t_2) - \Delta\alpha(t_1) = \frac{b}{2} \left(|t_2| - |t_1| \right) \tag{8}$$

where t_1 and t_2 correspond to the acceptance limits. The parameter a is not relevant since the Monte Carlo is normalized to the data.

The effective slope defined in (7) is slightly variable for the different data samples, since their average centre-of-mass energy varies. To take this into account when combining the results we define b in (7) as:

$$b = b^* \frac{\Delta t^*}{\Delta t} \tag{9}$$

where Δt is the actual energy-dependent t range and Δt^* corresponds to a reference centre-of-mass energy $\sqrt{s} = 91.1$ GeV. Then we fit for b^*.

With the acceptance cuts specified in section 4 the reference t range is: $t^*_1 = -1.78$ GeV^2, $t^*_2 = -5.96$ GeV^2, $\Delta t^* = |t^*_2| - |t^*_1| = 4.18$ GeV^2. The expected value of the effective slope in this t range is: $b = 223 \times 10^{-5}/\mathrm{GeV}^2$. It is important to realize which systematic effects could mimic the expected running or disturb the measurement. The most harmful effects are biases in the radial coordinate. Most simply one could think of dividing the detector acceptance in two and determine the slope with only two bins. In such a conservative model the running is equivalent to a bias in the central division of 70 microns. Biases on the inner or outer radial cut have less importance and could mimic the running for respectively 90 or 210 microns. Concerning radial metrology, an error of 0.5 mm on the inner radius would give the same observable slope as the running. Knowledge of the beam parameters, particularly the transverse offset and the beam divergence, is also quite important.

3 Detector, data samples and Monte Carlo simulation

The OPAL detector and trigger have been described in detail elsewhere [17]. In particular this analysis is based on the silicon-tungsten luminometer (SiW), which was used to determine the luminosity from the counting rate of accepted Bhabha events, from 1993 until the end of

LEP running. The SiW was designed to improve the precision of the luminosity measurement to better than 1 per mille. In fact it achieved a fractional experimental systematic error of 3.4×10^{-4}. The detector and the luminosity measurement are extensively described in [12]. Here we only review briefly the detector aspects relevant for this analysis.

The OPAL SiW luminometer consists of 2 identical cylindrical calorimeters, encircling the beam pipe symmetrically at about ± 2.5 m from the interaction point. Each calorimeter is a stack of 19 silicon layers interleaved with 18 tungsten plates, with a sensitive depth of 14 cm, representing 22 radiation lengths (X_0). The first 14 tungsten plates are each 1 X_0 thick, while the last 4 are each 2 X_0 thick. The sensitive area fully covers radii between 6.2 and 14.2 cm from the beam axis. Each detector layer is segmented with $R - \phi$ geometry in a 32×32 pad array. The pad size is 2.5 mm radially and 11.25 degrees in azimuth. In total the whole luminometer has 38,912 readout channels corresponding to the individual silicon pads. The calibration was studied with electrical pulses generated both on the readout chips and on the front-end boards, as well as with ionization signals generated in the silicon using test beams and laboratory sources. Overall pad-to-pad gain variations were within 1%. Particles originating at the interaction point had to traverse the material constituting the beam pipe and its support structures as well as cables from inner detector components before reaching the face of the SiW calorimeters. The distribution of this material upstream of the calorimeters is shown in Fig. 1. The material thickness was kept at a minimum especially in the crucial region of the inner acceptance cut where it amounts to 0.25 X_0, while in the middle of the acceptance it increases to about 2 X_0. Controlling and correcting the possible biases in the reconstructed position caused by this material was one of the most important aspects of this analysis and is addressed in the following sections.

We use the data samples collected in 1993-95 at energies close to the Z resonance peak. In total they amount to 101 pb^{-1} of OPAL data, corresponding to 12.0×10^6 accepted small angle Bhabha events. When LEP2 data-taking started in 1996 the detector configuration changed, with the installation of tungsten shields designed to protect the inner tracking detectors from synchrotron radiation. These introduced about 50 radiation lengths of material in front of the calorimeters between 26 and 33 mrad from the beam axis, thus reducing the useful acceptance of the detector at the lower polar angle limit. Moreover the new fiducial acceptance cut fell right in the middle of the previous acceptance, where the preshowering material was maximum. For these reasons we have limited this analysis to the LEP1 data samples.

The OPAL SiW detector simulation does not rely on a detailed physical simulation of electromagnetic showers in the detector. Instead it is based on a parameterization of the detector response obtained from the data [12]. This approach gives a much more reliable description of the tails of the detector response functions, which are primarily due to extreme fluctuations in shower development, than we could obtain using any existing program which attempts to simulate the basic interactions of electrons and photons in matter. The measured LEP beam size and divergence, as well as the measured offset and tilt of the beam with respect to the calorimeters are also incorporated in this simulation. The Monte Carlo simulation is used to correct the acceptance for the effects of the detector energy response, the coordinate resolution and LEP beam parameters. We divided the data into nine subsamples, depending on the year and the centre-of-mass energy, and generated an independent sample of BHLUMI events corresponding to each one of them, using a slightly different set of parameters in each case. The statistics were always at least 10 times those of the corresponding data set.

There are other corrections which are not accounted for by the Monte Carlo simulation, but rather applied directly to the data. These take care of accidental background, detector metrology and most importantly biases in the reconstructed radial coordinate. The latter is crucial for this analysis and will be discussed in section 5.

4 Event selection

The event selection criteria can be classified into *isolation* cuts, which isolate a sample of pure Bhabha scattering events from the off-momentum background, and acceptance defining, or *definition* cuts. The isolation cuts are used to define a fiducial set of events which lie within the good acceptance of both calorimeters and are essentially background free. The definition cuts then select subsets of events from within the fiducial sample. Showers generated by incident electrons and photons are recognized as clusters in the calorimeters and their energies and coordinates determined. The fine segmentation of the detectors allows incident particles with separations greater than 1 cm to be individually reconstructed with good efficiency.

The coordinate system used throughout this paper is cylindrical, with the z-axis pointing along the direction of the electron beam, passing through the centers of the two calorimeter bores. The origin of the azimuthal coordinate, ϕ, is in the horizontal plane, towards the inside of the LEP ring. All radial coordinate measurements are projected to reference planes at a distance of ± 246.0225 cm from the nominal intersection point. These reference planes correspond to the nominal position of the silicon layers 7 X_0 deep in the two calorimeters.

The *isolation* cuts consist of the following requirements, imposed on (R_R,ϕ_R) and (R_L,ϕ_L), the radial and azimuthal coordinates of the highest energy cluster associated with the Bhabha event, in each of the right and left calorimeters, and on E_R and E_L, the total fiducial energy deposited by the Bhabha event in each of the two calorimeters, explicitly including any detected energy of radiated photons:

- Loose radial cut, right (left)
$$6.7 \text{ cm} < R_R < 13.7 \text{ cm}$$
$$(6.7 \text{ cm} < R_L < 13.7 \text{ cm})$$
- Acoplanarity cut
$$||\phi_R - \phi_L| - \pi| < 200 \text{ mrad}$$
- Acollinearity cut
$$|R_R - R_L| < 2.5 \text{ cm}$$
- Minimum energy cut, right (left)
$$E_R > 0.5 \cdot E_{beam}$$
$$(E_L > 0.5 \cdot E_{beam})$$
- Average energy cut
$$(E_R + E_L)/2 > 0.75 \cdot E_{beam}$$

Note that by defining the energy cuts relative to the beam energy, E_{beam}, the selection efficiency is largely independent of $\sqrt{s}$.

The acollinearity cut (which corresponds to approximately 10.4 mrad) is introduced in order to ensure that the acceptance for single radiative events is effectively determined geometrically and not by the explicit energy cuts.

The isolation cuts accept events in which the radial coordinate, on both the Right and the Left side, is more than two pad widths (0.5 cm) away from the edge of the sensitive area of the detector. The *definition* cuts, based solely on the reconstructed radial positions (R_R, R_L) of the two highest energy clusters, then require the radial position on either side to be at least two further pads towards the inside of the acceptance. For the correction procedure explained in section 5 we refer to one specific silicon layer, which can be varied with some freedom. The Right and Left definition cuts are chosen so as to correspond closely to radial pad boundaries in the same detector layer. When the chosen layer is the reference layer at 7 X_0, the definition cuts are:

- Right side $\qquad 7.2 \text{ cm} < R_R < 13.2 \text{ cm}$
- Left side $\qquad 7.2 \text{ cm} < R_L < 13.2 \text{ cm}$

Expressed in terms of polar angles, these cuts correspond to 29.257 and 53.602 mrad.

When alternative layers are chosen the acceptance cuts and all the radial bin boundaries appropriate to that layer are projected to the layer at 7 X_0. For example when using the layer at 4 X_0, $R_{min} = 7.2584$ cm and $R_{max} = 13.3071$ cm. This rebinning introduces small statistical fluctuations in our fits depending on the specific choice of the layer, and is applied to be most naturally connected with the correction procedure for the radial distribution.

The radial distributions after the isolation cuts are shown in Fig. 2 for the complete LEP1 statistics and compared to Monte Carlo distributions normalized to the same number of events. The agreement is good except in the central part, where effects of the preshowering material are expected. Their correction is described in the following section.

The acceptance specified by the definition cuts is 0.5 cm (corresponding to two radial pad widths) wider than what has been used to define the OPAL luminosity [12]. In this way we extend the lever arm for observation of the running. The compatibility of the added data is quite good as can be seen from Fig. 2, where each point corresponds to one pad width. The agreement has been quantified by determining the χ^2 increase obtained when the fit in the former default acceptance is extended by 2 or 3 pads at both the inner and outer radius. The $\Delta\chi^2$ is fully consistent with purely statistical fluctuations corresponding to the added degrees of freedom.

5 Radial coordinate correction

Limitation of systematic error in the reconstructed radial coordinate, and particularly the limitation of any variation in the error from bin to bin, is key to the current measurement. Two complementary strategies are used to determine the radius of showering particles incident on the luminometer. The first is to utilize the information from the large number of pads throughout the depth of the detector which record signals from the shower to form a single, continuous, shower coordinate. The second is to utilize the inherent pad structure of the detector. Here we rely on the fact that, on average, the pad with the maximum signal in any particular layer will contain the shower axis. The first strategy has the advantage of providing a continuous measurement of maximum resolution. It also offers maximum immunity from any

large deviations due to an anomaly in a single pad signal. The second has the advantage of maintaining a transparent relation with the basic symmetry conditions of the detector. We refer to the first, robust, method as using *uncorrected* coordinates. When information from the pad receiving the maximum signal in any particular layer is applied, we refer to the coordinate as being *corrected* or *anchored*.

Details of how the coordinates are found from the recorded pad information are found in [12], but the essentials are as follows:

- Radial triplets of pads about the peak of the shower profile in each layer of the detector are used to form a continuous radial coordinate for the shower in that layer. The algorithm preserves two symmetry conditions: If the two largest pad signals in the triplet are equal, the coordinate falls on the pad boundary. Secondly, if the signals on the two extreme pads of the triplet are equal, the coordinate falls at the centre of the central pad.
- Acceptable layer coordinates in layers 2 to 10 are projected onto the reference plane of the detector, layer 7, which lies near the average longitudinal shower maximum, and averaged.
- This average coordinate is then linearized, or smoothed, to remove residual non-linearities. The smoothing algorithm imposes the constraint that no coordinate is allowed to cross the radius of a pad boundary in the reference layer 7.
- Any violation of the basic symmetry constraints of the measurement which may have been introduced in the process of constructing the average shower coordinate is then limited by comparing, in the ensemble, the average coordinate with the maximum pad observed in a large number of layers. This final procedure is termed *anchoring* the coordinate.

For the luminosity measurement, the anchoring proceedure was essential in establishing the absolute radius of the crucial inner acceptance boundary. In the current analysis it becomes even more important, since it is also used to correct the acceptance for every bin of the radial distribution. For this reason we discuss it here in some detail.

5.1 Anchoring Corrections

As the radial position of the incoming particles is scanned across a radial pad boundary in a single layer, the probability for observing the largest pad signal above or below this boundary shifts rapidly, giving an image of the pad boundary as shown in Fig. 3. These plots are obtained from OPAL data taken in 1993-94 and refer to three radial pad boundaries in layer 4 X_0 of the Right calorimeter. Similar plots were also made for test beam data. The pad boundary images are modelled with an error function (a Gaussian convoluted with a step function), where the Gaussian width $\sigma_a = w_a/\sqrt{2}$ measures the resolution at the boundary, while the radial offset R_{off} measures the displacement of the observed step from the nominal pad boundary.

From Fig. 3 one can see that the width is similar at the inner and outer radius, while it is considerably greater at the central radius. The offset R_{off} is found to be quite small at the inner edge while it increases to $\approx 10 - 20$ μm at the central and the outer radius.

Despite our reliance on the essential symmetry condition of the reconstruction, in reality this symmetry is slightly violated due to the $R-\phi$ geometry of the pads, and the corresponding increase of pad area with radius. As a result, the mean position of an ensemble of showers which share energy equally between two adjacent pads will actually lie at a smaller radius than the pad boundary. This is termed the *pad boundary bias*, $\delta R_{R\phi}$, and depends on the lateral extent of the shower. The pad boundary bias has been measured in a test beam and parametrized as a function of the apparent width of the shower, w_a, and varies from essentially zero to about 20 μm.

An additional, second order, effect also arises whenever a cut is imposed on a quantity with a steeply falling distribution, such as the radial Bhabha spectrum. An acceptance change is introduced due to the fact that more events actually on the uphill side of the cut will be measured to fall on the downhill side than vice–versa. This *resolution flow*, δR_{res}, is a small (positive) additional bias which can be expressed as:

$$\frac{\delta A}{A} = \frac{\mathrm{d}f}{\mathrm{d}x}\frac{\sigma_x^2}{2} \tag{10}$$

where $f(x)$ is the intensity of events normalized to unity over the considered acceptance A, and σ_x is the resolution in the variable x upon which the cut is imposed. For our measurement the relative acceptance change varies from almost zero to about 1.5×10^{-4}, corresponding to a δR_{res} of about 8 μm.

The total net bias in the uncorrected coordinate, δR (also called *anchor*), as determined by the position of a pad boundary image is therefore given by:

$$\delta R = R_{off} + \delta R_{R\phi} + \delta R_{res} \tag{11}$$

where R_{off} is the observed offset of the pad boundary image, which may have positive or negative sign, while both $\delta R_{R\phi}$ and δR_{res} are always positive.

The anchors determined from 1993-94 data for the layers at 4 X_0 for all the pad boundaries used in the analysis are shown in Fig. 4. A similar trend is visible on the two sides, in particular the rise of the anchor from $5-10$ μm at the inner edge to $20-25$ μm around $R=9$ cm. The error bars include in quadrature the systematic errors from the fit method, pad gain variations, and the assumed $1/R$ scaling and shower width dependence of the pad boundary bias as discussed in Section 7.1. The inner error bars show the statistical errors in the fit of the pad boundary images. More details on errors assigned to the anchors can be found in [12]. The anchors determined from 1995 data have similar features although with lower statistics.

The anchors have been determined separately for 1993-94 and 1995 data, because the amount of preshowering material was different in the two sub-samples. A clear relation with the amount and distribution of the material upstream of the calorimeters is visible from the apparent width σ_a as a function of radius, as shown in Fig. 5. The noticeable difference between the Right and Left widths in 1993-94 data is due to the presence of cables from the OPAL microvertex detector. For 1995 data additional cables were installed in the Right side, which restored an almost symmetrical situation. The presence of a non-negligible amount of preshowering material in the middle of the acceptance constitutes the most delicate experimental problem for this analysis, since the anchoring procedure was developed and checked using the test beam only for the amount of preshowering material ($< 1\,X_0$) most relevant for the luminosity

measurement. We have therefore made extensive checks as described in Section 5.2 and 7.1 to identify a broad region within the detector where the anchoring procedure is valid, and derive our results using only the center of this region.

To use the anchors, we do not actually correct the measured shower coordinates themselves, but rather convert the anchors to appropriate acceptance corrections. The acceptance of an individual radial bin with boundaries ($R_{in},\ R_{out}$) is affected by the net biases of the edges $\delta R_{in},\ \delta R_{out}$ determined as in (11) according to the following formula, which gives the fractional acceptance variation:

$$\frac{\delta A}{A} = c_{in}\ \delta R_{in} - c_{out}\ \delta R_{out} \tag{12}$$

The coefficients c_{in} and c_{out} are derived by a simple analytical calculation assuming a $1/\theta^3$ spectrum for the angular distribution and are given by:

$$c_k = \frac{\frac{1}{R_k^3}}{\frac{1}{2}\left(\frac{1}{R_{in}^2} - \frac{1}{R_{out}^2}\right)} \qquad k = in, out \tag{13}$$

Whether we plot uncorrected coordinates or apply the anchoring corrections, we bin the radial distribution according to the nominal pad boundaries of a particular layer, projected onto the reference layer $7\,X_0$. The particular layer chosen is always the one used in determining the relevant anchors. These anchoring corrections are at most 0.5% for the Right and 1.0% for the Left side in 1993-94 data and correspondingly 0.8% and 0.7% in 1995 data.

5.2 Limitations in the Anchoring

Our strongest insurance against the presence of excess systematic error in the radial shower coordinate is to demand consistency between the corrected and uncorrected coordinates. As already mentioned, the uncorrected coordinates are robust, and derived from the signals observed on a large number of pads throughout the detector, while the corrected coordinates rest on observing equal signals, in the mean, inside and outside of an indivdual radial pad boundary in a particular detector layer. These corrected coordinates provide reliable benchmarks throughout most of the detector, but are expected to become fragile at both very shallow and very deep layers of the calorimeters, particularly in the region of the detector obscured by significant preshowering material.

Not only does the lateral shower profile broaden deep within the calorimeter, but beyond shower maximum the energy in the shower also becomes smaller. Both these effects make determination of the pad boundary transition increasingly subject to disturbance. At shallow depths, particularly behind preshowering material located considerably upstream of the detector, a shower can frequently develop a long, asymmetric tail which can lead to a significantly non-Gaussian error in the position determined in a single layer.

The pad boundary bias was determined in the test beam behind a maximum of 0.84 X_0 of preradiating material. Under such conditions, and at reasonable depths, we determined that the pad boundary bias could be adequately parametrized as a function of the apparent shower width alone. Behind greater amounts of preshowering material, the validity of this simplification may break down, and we can expect that an additional, explicit, depth dependence may become

necessary to adequately describe the pad boundary bias at both very shallow and very deep layers within the calorimeter.

We therefore compared the corrected and uncorrected coordinates as a function of the layer used for the anchoring to expose such effects. As expected, significant deviations are observed at both very shallow and very deep layers, particularly on the Left side in the 1993-4 data, where the the pre-showering material was greatest.

The uncorrectd radial coordinate can be studied by simultaneously varying the value of the radial cut in the data and in the Monte Carlo. The Monte Carlo here assumes the expected running of α and that the radial coordinate is reconstructed without bias. Thus differences in the acceptance of the data and Monte Carlo as the radial cut is varied, beyond those expected from the finite statistics and any departure from the expected running of α, can indicate biases in the radial coordinate. Letting $\Delta A = A(R; R_{out}) - A(R_{in}; R_{out})$ be the acceptance change obtained by moving the inner radial cut to any given position R, and setting $A_{data}(R_{in}; R_{out}) = A_{MC}(R_{in}; R_{out})$ to disregard the integral normalization, we form the quantity:

$$\left(\frac{\Delta A}{A}\right)_{data} - \left(\frac{\Delta A}{A}\right)_{MC} = \frac{A_{data}(R; R_{out}) - A_{MC}(R; R_{out})}{A_{data}(R_{in}; R_{out})} \tag{14}$$

This relative acceptance, as a function of R is shown as a shaded band (the lower one) for the Right and the Left side selection in Fig. 6 for 1993-94 data. The width of the bands represents the binomial errors with respect to the reference selection 7.20 cm $\leq R \leq$ 13.20 cm. Note that, by construction, both ends of the relative acceptance band at $R = 7.2$ cm and $R = 13.2$ cm are required to lie at zero.

The solid points show the anchoring results for all the relevant pad boundaries in layers between 1 X_0 and 10 X_0. The radial bias corresponding to each anchor is converted into an acceptance variation using the formula:

$$\frac{\delta A}{A} = 2\ \frac{R_{in}^2 R_{out}^2}{R_{out}^2 - R_{in}^2}\ \frac{\delta R}{R^3} \tag{15}$$

where $R_{in} = 7.20$ cm, $R_{out} = 13.20$ cm and R is varied from R_{in} to R_{out}. Since the normalization is the total acceptance, the low R points have a greater weight in the plot, due to the $1/R^3$ dependence. Therefore any visible structure tends to be flattened at increasing radius. Any of the anchors can be chosen to fix the absolute offset in the continuous radial coordinate, here we choose the anchor at $R = 7.20$ cm in layer 7 X_0 and this point correspondingly lies at zero.

Each group of nearby points, marked by either circles or triangles, refer to a given radial pad boundary in different layers, that is at variable depth in the calorimeters. Since all the coordinates are projected to the reference layer 7 X_0, the corresponding pad boundaries in adjacent layers differ by about 200 μm at the inner radius and by about 350 μm at the outer radius after projection. The arrows mark the position of a given pad boundary in layer 7 X_0, deeper layers have a lower R and shallower layers a higher R. Note that in contrast to the acceptance bands also shown in this figure, these anchoring points are independent of the Monte Carlo, and do not depend on the assumed running of α.

The essential point of Fig. 6 is that the anchor points derived from individual pad boundaries should follow the relative acceptance band derived from the distribution of coordinates, since this shows that the two independent methods of determining shower positions in the calorimeter

are in agreement. It must also be remembered that the choice of which anchor to use in fixing the global offset of the radial coordinate is arbitrary. Almost all anchors are found to be consistent, even in those regions where the relative acceptance band reveals the presence of residual structure in the coordinate. However, clear discrepancies are apparent for the deepest layers considered ($8-10\ X_0$), in particular for the Left side. This is most evident in the central region of acceptance, where the amount of material between the detector and the interaction point is large and the parametrization of the expected bias derived from the test beam is evidently no longer applicable. The behavior of the anchors with depth indicates that the onset of these problems is abrupt, and a large region of the detector remains well understood for use in our analysis. Notice that in the obscured region of the detector the run-away of the anchors occurs almost exactly one layer earlier on the Left side of the detector, at layer 8 X_0 than it does on the Right, indicating that the 0.5 X_0 of additional preshowering material has an effect larger than an equivalent amount of compact absorbing material in the detector. We have therefore selected layer 4 X_0 as the central layer for anchoring, and checked the results with alternative anchors from layer 1 X_0 to layer 7 X_0.

This comparison of the uncorrected data and Monte Carlo depends on the running of α that we want to measure, so the remarkably flat shape of the relative acceptance means that the data agrees with the input $\alpha(t)$ in the Monte Carlo. To make this clear we have also plotted the prediction for zero running as the hatched bands. The highly significant "eyebrow" shape of the zero-running acceptance bands, and their clear separation from the flat Standard Model bands is a graphic representation of our measurement's sensitivity.

The run-away anchors in the deepest layers considered are consistent with the eyebrows, however, and show that the effects of the preshowering material for these deep layers, particularly on the Left side, would give an apparent shape consistent with zero running. As mentioned previously this is equivalent to biases of about 70 μm in the middle of the acceptance.

6 Finding Safe Anchors for the Measurement

In order to see more directly the effect of anchoring imperfections on the slope of the running which we wish to measure, we have made a series of test fits to determine the running slope, b^*, for each choice of anchoring layer. The fits are simple χ^2 fits of the ratio of data to Monte Carlo events observed in each bin to the two coeficients of Equation 7. The Monte Carlo in this case assumes a constant value of α: $\alpha(t) \equiv \alpha_0$. Since anchoring problems may manifest themselves either as increased fluctuations from bin to bin, or as broader, more dangerous, systematic effects highly correlated between nearby bins, we pursue two lines of investigation.

In the first we study the stability of the anchors at individual pad boundaries. To do so, we divide the radial distribution into the maximum number of bins: at each layer a bin corresponds to each of the 24 pads in the fiducial region. Since the assesed systematic errors are somewhat correlated from bin to bin, we consider only statistical errors, which are in any case dominant. To isolate the effects associated with the anchors, we focus on the difference in χ^2 between the corrected and uncorrected distributions.

Fig. 9 shows the difference between corrected and uncorrected χ^2 (d.o.f.=22) as a function of the anchoring layer. It is apparent that beyond layer 7 X_0 the χ^2 becomes progressively worse.

By considering the (cleanest) 1993-94 data on the Right side, the anchoring improves the χ^2 in layers $1-6\ X_0$. These results indicate that the anchors deeper than layer 6 X_0 suffer from fluctuations significantly larger than the inherent statistical uncertainties, and therefore are not suitable for use in the measurement. On the other hand, the anchor fluctuations in layers $1-6\ X_0$ are smaller than the information they confer, and therefore appear safe.

In the second study, we focus on broader systematic effects which have a direct effect on the measured running. Here we optimise the number of bins for extraction of the running slope, as specified in Table 7 (for layer 4 X_0). This binning is more consistent with the small number of parameters we wish to extract, the bin width grows with increasing radius to compensate the diminishing statistics, and any noise associated with fluctuations at the supressed intermediate bin boundaries, which we treated in our first study, is reduced. Here, in addition to the statistical errors, we also include the full matrix of systematic errors which is specified in Table 9. The fit values of b^* for each layer are shown in Fig. 8. The results are shown separately for the two sides, and for the two homogeneous data sets, 1993-4 and 1995. The uncorrected slope shows only small statistical fluctuations due to the rebinning in each layer. The corrected slope is close to the uncorrected result in layers $1-6\ X_0$, then shows a steady decrease with increasing depth in the calorimeters. Layer 0 X_0 shows a strong deviation from the uncorrected result, in the opposite sense. Consistent with Figure 6, for 1993-4 data the deviation on the Left side preceeds that on the Right by almost exactly one layer, due to the presence of the extra preshowering material of the microvertex cables. In the 1995 data the observed deviations are similar on the two sides, reflecting the fact that the preshowering material is then symmetric.

These results indicate that the corrected values of b^* are consistent with the uncorrected values, within the assigned systematic error, for the broad region covering layers $1-6\ X_0$. This is true for both sides, and for all datasets.

Nonetheless, the Left side appears to exhibit a pattern of deviations consistent with a residual depth-dependent effect, particularly in the more statistically significant 1993-4 data. Due to the back-to-back nature of Bhabha events, the two sides do not contribute independent statistical information about the running. We therefore choose to derive our final results from the Right side alone. Even though in 1995 the Right data is affected by extra preshowering material to an extent similar to the 1993-4 Left data, we consider that the gain of statistical precision in using this data outweighs the risk of any potential increase in systematic error. We also choose the anchors in layer 4 X_0 to correct our final results, since this layer lies in the center of the safe region, where the corrected and uncorrected results are most consistant. In some sense this decision is simply prophylactic: all results within the safe anchoring region are consistent within the assigned errors, corrected and uncorrected, on both sides of the detector, and for all datasets.

7 Systematic uncertainties

Having discussed how we ensure that our anchoring corrections are chosen from a safe region of the detector, we now quantify the residual errors we attribute to these anchors, as well as all other systematic errors we identify as affecting the measurement. The analysis of these errors closely follows their treatment in the SiW luminosity analysis [12]. The discussion here focuses

on those considerations specific to the current measurement, and quantifies their effect on the extracted value of b^*. The systematic uncertainties are grouped into classes, summarized in Table 4, and discussed in detail below.

7.1 Anchoring errors

This error class includes all the uncertainties connected with the anchoring procedure described in section 5. Biases on the radial coordinate can directly affect the shape of the t distribution. In particular a bias on the reconstructed position in the central part of the acceptance, behind the dead material, can produce a significant error. As mentioned in Section 2, a bias in the central region of 70 μm would double the expected apparent running or reduce it to zero depending on the sign of the bias.

Shifts in the anchors can arise either through the measured value of R_{off} or through the determination of the pad boundary bias, $\delta R_{R\phi}$. The measurement of R_{off} is affected by pad gain fluctuations and departures from the Gaussian model used for extracting the pad boundary image. A global uncertainty in $\delta R_{R\phi}$ has negligable effect on the current measurement, but uncertainty in its radial dependence must be considered.

The observed R_{off} is affected by fluctuations in the individual pad gains. We have checked these effects directly on data, by studying R_{off} for each of the 32 azimuthal divisions of the calorimeters. We assign the statistically expected shift in the mean caused by the azimuthal variations, $(R_{off})_{RMS}/\sqrt{32}$, as a systematic error in the anchors, due to pad gain variations. *(rgk: We need to quantify the contribution of this error component)*

Fig. 3 shows that a Gaussian resolution does not perfectly describe the tails of the distribution from which we extract the pad boundary image. To the extent that this image maintains an odd symmetry about the apparent pad boundary, its non-Gaussian behaviour does not affect the determination of R_{off} as can be seen from the close agreement of the data points and the fitted curve near the pad boundary. We have also considered a model in which the apparent pad boundary is taken as the median of the observed resolution function. The difference between the two models is assigned as a systematic error of the fit method, when it is larger than the fit statistical error, otherwise the latter is kept as the estimated error. *(rgk: We need to quantify the contribution of this error component)*

The determination of the pad boundary bias in the test beam was carried out at a radial position close to the inner acceptance cut to provide optimal information for the luminosity determination. In this analysis we have a greater dependence on knowing the pad boundary bias throughout the detector. The geometrical bias due to $R-\phi$ pads is expected to scale as $1/R$, thus decreasing at a greater radius of pad curvature. Therefore we have scaled the bias estimated using the test beam results, but assign an additional systematic error equal to 50% of the expected bias to account for possible deviations from this behaviour. *(rgk: We need to quantify the contribution of this error component)*

These uncertainties have been incorporated in the covariance matrix and their effect on the fitted slope have been assessed. *(rgk: Whoa, the text seems to contradict itself concerning whether the anchoring errors are included in the covariance matrix, or whether they are taken as additional contributions to the fit error. This must be clarified)* These uncertainties have been

taken as additional quadratic contributions to the fit error and have been determined separately for the 1993-94 and 1995 data. We obtain $11(13) \times 10^{-5}/\mathrm{GeV}^2$ for the Right (Left) side in 1993-94 data and $13(18) \times 10^{-5}/\mathrm{GeV}^2$ for the Right (Left) side in 1995 data, corresponding to an effective anchoring error of about 4 μm.

7.2 Dead material

To cover in a conservative way possible effects of the dead material we did a few direct tests using the data itself. The amount of preshowering material is maximum in the middle of the accepted radial range, as is reflected in the σ_a distribution shown in Figure 5. We have thus defined two regions:

- CLEAN region, $R \leq 8.2$ cm and $R \geq 11.7$ cm, corresponding to the first 4 pads starting from the inner radial cut and the last 6 pads close to the outer cut;
- OBSCURED region, $8.2 < R < 11.7$ cm, corresponding to the central 14 pads.

The fitted slopes determined separately in the two regions are given in Table 3. We see that the results obtained in the CLEAN region are quite close to the results of the fit on the full acceptance, given in Tables 1-2. *(rgk: Tables 1-2 could be dropped if the total acceptance result is added to Table 3)* Moreover the independent values obtained in the OBSCURED region are consistent within the statistical errors. It is natural to expect a possible extra pad boundary bias in the bad region, particularly on the Left side. We have checked for its presence, by introducing a new parameter x in the fit, related to this assumed extra bias using two alternative models:

- *Box-model*, a naive choice assuming a constant extra bias within the bad radial region and no extra bias outside it. Here x is the constant extra bias.
- *W-model*, the extra bias δR_{extra} is assumed to follow the pattern of the apparent shower width σ_a versus R:

$$\delta R_{extra} = x \frac{\sigma_a(R) - \sigma_a(R_{in})}{\sigma_{max} - \sigma_a(R_{in})} \tag{16}$$

  where R_{in} is the inner acceptance cut, where σ_a is minimum, and σ_{max} is the maximum value of σ_a, which is reached near the centre of the detector ($R \approx 10.2$ cm). So $\delta R_{extra} = x$ when $\sigma_a(R) = \sigma_{max}$.

No evidence for an extra bias is found under either of the two hypotheses. We take the statistical sensitivity of the check as a systematic uncertainty, quantified as the additional contribution to the error on the slope generated by allowing the possibility that such an extra bias might exist. We obtain $10(18) \times 10^{-5}/GeV^2$ for the Right (Left) side in 1993-94 data and $27(30) \times 10^{-5}/GeV^2$ for the Right (Left) side in 1995 data. Notice that such uncertainties cover the observed shifts between fits in the restricted CLEAN region and in the full acceptance in each of the various cases.

The estimated error for the Left side is about twice that for the Right side in 1993-94 data.

7.3 Position resolution

The radial resolution at pad boundaries in the clean acceptance near the inner edge of the detector has been measured using the test beam to be 130 μm. The apparent resolution at the outer edge and in the central portion of the detector, behind the bulk of the preshowering material, is degraded approximately by a factor of 2 to 2.5, according to the pattern of Figure 5. The Monte Carlo simulation includes a radial dependence accounting for this variation. The impact of any unaccounted degradation of the radial resolution as a function of radius is tiny. For example, to get an effect the same size as the running, the resolution behind the material would have to be wrong by 2 mm. We conservatively assessed the uncertainty related to the radial resolution by dividing the acceptance into two radial bins and calculating the full effect of the resolution flow on the slope. It amounts to $4(10) \times 10^{-5}/\mathrm{GeV}^2$ for the Right (Left) side in 1993-94 data and $7(9) \times 10^{-5}/\mathrm{GeV}^2$ for the Right (Left) side in 1995 data. The contribution of the resolution flow across the acollinearity cuts is negligible in comparison, amounting to $1 \times 10^{-5}/\mathrm{GeV}^2$ in all cases.

The resolution on the reconstructed azimuthal coordinate is not critical because of the cylindrical symmetry of the detector. It only enters through the cuts on the acoplanarity distribution as a resolution flow effect, which is taken into account by the detector simulation. Radial variation of the azimuthal resolution and unaccounted non-Gaussian tails give uncertainties on the slope smaller than $10^{-5}/\mathrm{GeV}^2$ and have been neglected.

7.4 Acollinearity bias

The acollinearity distribution, with the selection cuts $|\Delta R| \leq 2.5$ cm, is not corrected using anchors as is the radial distribution. Therefore it is subject to biases of the order of the anchors themselves. In the worst case there could be a first order effect causing a net gain or loss of events at both the positive and the negative ΔR cut. This is conservatively estimated by considering a bias with absolute value $\Delta R_{bias} = 30$ μm, which is the maximum reached by the anchors. This corresponds to an uncertainty on the slope of $3 \times 10^{-5}/\mathrm{GeV}^2$.

7.5 Metrology

The detector geometry was carefully determined and monitored for the luminosity measurement [12]. The most crucial quantity in that analysis was the inner radius of the calorimeters, since the internal geometry of the Si wafers is inherently excellent. This analysis is much less sensitive to the absolute radial scale, and it would require a radial shift of about 0.5 mm to mimic the expected α running. Even without averaging over the measurements of the two sides, the inner radii are known with a precision of 7μm, which gives an error on the slope of only $3 \times 10^{-5}/\mathrm{GeV}^2$.

In operating conditions the thermal effects also contributed variations to the nominal radial dimensions of the detector on the order of $2 - 10\mu$m. These were calculated independently for each data set, according to the average temperature measured by thermistors located on each detector layer. Such thermal effects give contributions to the slope of $1 - 4 \times 10^{-5}/\mathrm{GeV}^2$, which have been considered correlated between all the data samples.

This analysis is insensitive to longitudinal metrology errors. In fact an error in the longitudinal separation between the Right and Left calorimeters would be equivalent to a shift in the z position of the interaction vertex which has no effect on the slope. Also the inter–layer separation gives negligible uncertainties: for a change of 100μm in the spacing between layers, the effect on the slope is below $10^{-5}/\mathrm{GeV}^2$ for all layers considered $(1 - 10X_0)$.

7.6 Beam parameters

The geometry of the colliding beams with respect to the detector can have quite important effects on the apparent slope. The size of the running is comparable to the effect of an uncorrected transverse offset of the beams of 4 mm or a beam angular divergence of 1.4 mrad. These values are much larger than those we experienced. Moreover we were able to safely determine such parameters from the data.

The uncertainties related to the beam parameters are geometric effects which modify the radial acceptance and can be adequately calculated analytically by assuming a simple $1/\theta^3$ angular distribution. Here, with regard to the slope of the radial distribution, it is enough to work out the estimates by dividing the radial acceptance into two bins. In this way one gets a conservative estimate, since the isolation cuts, which are neglected analytically, considerably decrease the variations calculated from the acceptance cuts alone.

The transverse beam offset is measured run-by-run with a precision better than 10 μm and gives a negligible uncertainty on the fitted slope. The beam tilt is the most important effect. Its two components are determined run-by-run as the difference of the eccentricities of the unscattered beams as they pass through the bore of each calorimeter. These eccentricities are measured by the azimuthal modulation of the Bhabha intensity, and the statistical accuracy with which they can be determined is $200 - 300$ μm for typical runs. For the nine data sets the beam tilt contributes $1 - 3 \times 10^{-5}/\mathrm{GeV}^2$ to the uncertainty in the slope. These errors have been conservatively taken twice: both correlated and uncorrelated. To cover the possibility of rapid tilt variations, on a time scale shorter than an individual run, we have conservatively taken as an additional uncertainty the slope variation corresponding to setting the beam tilt to zero. Note that random variations in the angles of the electron and positron beams will appear as additional contributions to the beam divergence, which is considered as an independent parameter. In order for the tilts to have an effect on the acceptance which is not included in the divergence correction, the trajectories of the incoming positron and electron beams must change in a correlated manner. They range from $1 \times 10^{-5}/\mathrm{GeV}^2$ for the largest sample (94-b) to $10 \times 10^{-5}/\mathrm{GeV}^2$ in the worst cases. We have taken such numbers as uncorrelated errors, with an additional common correlated systematic equal to $1 \times 10^{-5}/\mathrm{GeV}^2$.

The transverse beam size and divergence give effects similar to the radial resolution. They can be calculated by expressing the radial acceptance variation due to the resolution flow. The uncertainty due to the beam size is conservatively estimated by taking the full size of the effect: its contribution to the slope is below $1 \times 10^{-5}/\mathrm{GeV}^2$ and has been neglected. The uncertainty on the beam divergence, estimated by comparing two independent determinations, ranges from $\approx$ 100 μrad for 1993-94 data and $\approx$ 130 μrad for 1995 data. The resulting uncertainty on the slope is $1 \times 10^{-5}/\mathrm{GeV}^2$ and $2 \times 10^{-5}/\mathrm{GeV}^2$ respectively. We have taken these errors as uncorrelated but additionally a correlated term equal to 1×10^{-5} has been considered.

The longitudinal position of the beam spot has a constant effect on the radial acceptance so gives no contribution to the slope. The same holds for the longitudinal size of the beam spot.

The uncertainties estimated in this way have been checked with the results of Monte Carlo simulations where one parameter at a time can be varied. In this case the isolation cuts are included, at the price of some statistical limitation. The results are consistent.

7.7 Energy Response

The essential problem here is how the pre-showering material degrades the energy response and causes events to be lost from the accepted sample. Uncertainties due to the energy response have been assessed by varying the parameters in the detector simulation within the precision they have been estimated from the data. They include the Gaussian width of the energy response function, the exponential low-energy tail, the nonlinearity and the method used to extrapolate the energy resolution to lower energies. We determined the variation in the fitted slope in a conservative way, by dividing the radial acceptance into two bins and then by changing in turn each parameter in the simulation of the outer bin, leaving unchanged the parameters for the inner bin. Then we took the sum in quadrature of all the variations. The dominant uncertainty is caused by the low-energy tail of the response function, which is generated by events that shower very late in the detector, events not fully contained and events with electrons and positrons that scatter off upstream material. The resulting uncertainty is $8 \times 10^{-5}/\mathrm{GeV}^2$ for both the Right and the Left calorimeter.

7.8 Accidental background

Off-momentum electrons and positrons generated by beam-gas scattering generate the majority of single showers in the luminometer. Accidental coincidences between background clusters in the Right and Left calorimeters can occasionally produce events which are selected as Bhabha scatterings, although in general these events are rejected by the minimum energy cuts or fail the acollinearity cuts. This background was studied by special triggers including random bunch crossings and delayed coincidences. The background fractions were found to vary between 0.1 and 0.6×10^{-4} depending on the data set [12]. We have conservatively estimated the effect on the slope by dividing the acceptance into two radial bins and assuming that the background is concentrated in the inner bin. The radial distribution of background is indeed sharply peaked at low radius. To account for the enlarged acceptance used in this analysis we increased the background fractions by 50 %, which covers the variations observed by studies of the background distributions. The effect on the slope is a slight decrease between 1 and $5 \times 10^{-5}/\mathrm{GeV}^2$ which has not been corrected but taken as an uncertainty correlated between the data samples.

The accidental overlap of a background cluster with a Bhabha event can also change the values of reconstructed quantities, modifying the acceptance. This has been evaluated by incorporating the measured background into the detector simulation, by adding to BHLUMI events background clusters with rates determined from random triggers. Likewise we have also combined the measured background with data. In both cases the resulting shift in the slope is smaller than $10^{-5}/\mathrm{GeV}^2$ and has been neglected.

7.9 Biases of the method

The reconstructed t has a small positive bias, due to initial-state radiation, with respect to the exchanged four-momentum between the electron and positron line. From a study of BHLUMI Monte Carlo events this is found to be almost zero at the inner acceptance cut, increasing to about 0.1 GeV^2 at the outer cut. If we were to correct the average t values for this radiation, it would give a small increase of the slope by $+5 \times 10^{-5}/\mathrm{GeV}^2$. The corresponding small reduction of the t range, however, acts to cancel this effect when determining the variation of the coupling from equation (8). Therefore we have not corrected the slope for this effect and neglected its small uncertainty.

The linear approximation to the t dependence expressed by equation (7) has been checked with a theoretically–based logarithmic dependence for the running of the effective coupling. We have no statistical sensitivity to deviations from linearity, although the linear approximation results in a small positive bias with respect to the assumed logarithmic dependence. This has been studied by Monte Carlo and is $+12 \times 10^{-5}/\mathrm{GeV}^2$ on the b slope at peak energy, taken as a fully correlated systematic uncertainty. For off-peak data sets this is convoluted with effects of Z interference to give slightly different values depending on energy, as reported in table 4.

7.10 Summary of systematic errors

The dominant systematic errors are those related to anchoring and dead material, described in sections 7.1 and 7.2.

The experimental systematic uncertainties are summarized in Table 4. The final experimental error correlation matrix (including the statistical errors) is given in Table 5. The correlations reach at most 10 %. The classification of the detailed sources of error into correlated and uncorrelated components given in Table 4 does not reveal the complete pattern of correlations embodied in the full correlation matrix. In that table the errors classified as correlated are fully correlated between all data samples, while those classified as uncorrelated are often correlated within a given year, but uncorrelated between years.

8 Theoretical uncertainties

It is important to assess the theoretical uncertainties implied by the BHLUMI Monte Carlo. In fact a reliable determination of the running coupling constant from equation (2) needs a precise knowledge of the radiative corrections.

The theoretical uncertainty of the BHLUMI calculation of small angle Bhabha scattering has been extensively studied for the event selections of LEP experiments. The fractional theoretical error is 6.1×10^{-4} for the integrated cross section at LEP1 energy [13, 18] which was relevant for the determination of the integrated luminosity. Alternative existing calculations have been widely cross-checked with BHLUMI [13]. Moreover the extensive comparisons between data and the predictions of many features predicted by the Monte Carlo by the four LEP collaborations decrease the chances that it contains significant residual technical imperfections. Therefore

the estimate of the theoretical uncertainty of BHLUMI is solid. BHLUMI does not include diagrams with extra light pairs ($e^+e^-, \mu^+\mu^-$). Their contribution was calculated explicitly for the (idealized) OPAL acceptance, giving a fractional correction of $-4.4 \pm 1.4 \times 10^{-4}$ [19]. With this correction the theoretical error on the OPAL integrated luminosity was reduced to 5.4×10^{-4}, dominated by uncertainties on vacuum polarization and photonic corrections.

We have studied the uncertainty on the slope of the differential cross section in a conservative way, by degrading the precision of BHLUMI for the last perturbative order. Since BHLUMI includes completely the $\mathcal{O}(\alpha^2 L^2)$ terms, we have compared it to the exact $\mathcal{O}(\alpha)$ calculation of the former OLDBIS Monte Carlo programme [20]. This is based on the calculation of an independent group [21], but is included within the BHLUMI package. Thus this check also covers aspects of the technical precision. BHLUMI gives access to many intermediate weights which compose the final calculation, so that we could also check several different approximations.

We did this study by using a slightly modified version of the idealized model of the OPAL detector, which is contained in the BHLUMI package (subroutine TRIOSIW). We generated the events within a safely enlarged angular region to protect against loss of visible events. This code was used also for the work of [13]. Smearing effects are neglected and an ideal beam is assumed. Nearby particles are combined by a clustering algorithm which has a window matched to the experimental resolution. The energy is defined by summing all the particles inside the isolation cuts on each calorimeter. The position variables R and ϕ are defined as the coordinates of the highest energy particle reconstructed on each side. We applied all the isolation cuts listed in section 4 to these reconstructed variables. The differential cross section obtained at different perturbative orders is shown in Figure 10 normalized to the reference BHLUMI cross section. Here vacuum polarization, Z-exchange interference and s-channel photon interference have been switched off. The Born cross section is reduced by about $5 - 15$ % by radiative corrections, depending on the polar angle. The cross section at $\mathcal{O}(\alpha)$ is slightly lower than the reference but in general agrees within 1 %, except for the upper edge of the angular acceptance where the difference is close to 2 %. The $\mathcal{O}(\alpha)_{exp}$ calculation is almost identical to the reference.

We fit the ratio of calculations at different orders and determine the shift in the slope, δb, which corresponds to using these alternatives as the reference for our fit to the data. The results are shown in Figure 11 and are:

$$OLBIS[\mathcal{O}(\alpha)]/BHLUMI \Rightarrow \delta b = -29 \pm 21 \times 10^{-5}/GeV^2$$
$$\mathcal{O}(\alpha)_{exp}/BHLUMI \Rightarrow \delta b = +6 \pm 13 \times 10^{-5}/GeV^2$$

We take half the result of the $OLBIS[\mathcal{O}(\alpha)]$/BHLUMI fit as a conservative estimate of the systematic error related to neglected photonic corrections ($14 \times 10^{-5}/\mathrm{GeV}^2$). The size of the window used by the cluster algorithm (on R and ϕ) has been varied over a large range to verify the stability of the result. The result of the $\mathcal{O}(\alpha)$/BHLUMI fit moves at most by $3 \times 10^{-5}/\mathrm{GeV}^2$, while the $\mathcal{O}(\alpha)_{exp}$/BHLUMI fit is unchanged. We point out that the acollinearity cut applied by our selection is very effective in reducing the importance of the photonic radiative corrections. An alternative idealized selection (similar to the ALEPH standard selection, named SICAL in [13]) without such a cut would result in a systematic error of $25 \times 10^{-5}/\mathrm{GeV}^2$ according to the same procedure.

The interference with the Z exchange amplitude in the s-channel is a small correction, designated δ_Z in equation (2), which is not factorized with respect to the main contribution and

the running coupling constant. It is energy dependent, vanishing at $\sqrt{s} = m_Z$ and changing sign across the Z mass. In BHLUMI it is calculated to $\mathcal{O}(\alpha)_{exp}$ with the vacuum polarization correction included. Alternatively it can be obtained to the same order but without the vacuum polarization correction, at the Leading-Log level or at the Born level. We have studied the effect of uncertainties on this piece by degrading the default calculation to the Born approximation for δ_Z. We generated large samples of events at three different energy points: the Z-peak energy (set to $\sqrt{s} = 91.1$ GeV) and energies offset by ± 2 GeV. Radiative corrections on Z interference are found to shift the fitted slope by $+31 \pm 15 \times 10^{-5}/\mathrm{GeV}^2$ at $\sqrt{s} = 89.1$ GeV and $-20 \pm 15 \times 10^{-5}/\mathrm{GeV}^2$ at $\sqrt{s} = 93.1$ GeV with respect to the result obtained with the Born calculation. We have checked also the effect of the inclusion of vacuum polarization in the δ_Z term, as this subtle effect could in principle perturb the asserted cleanliness of the measurement. We find $\pm 7 \times 10^{-5}/\mathrm{GeV}^2$ for the induced shifts on the fitted slope, much less than the effect of photonic corrections. The estimated theoretical uncertainties are summarized in Table 6.

9 Results

As explained in Section 6, our final results are based solely on the angular distribution observed in the Right calorimeter, and on radial coordiates corrected using the anchoring procedure described in Section 5. The back-to-back nature of Bhabha events implies that the two sides of the detector do not provide independent statistical information concerning the running of α, and the decision to use only the Right calorimeter is based on the desire to reduce possible unassessed systematic error. Similarly, the decision to use corrected coordinates has little import, since our faith in the anchoring requires consistency between the corrected and uncorrected results. Changing any of these choices would shift our result by no more than 10% of its error.

For our final fits the radial distribution is binned as specified by table 7. The numbers of data and Monte Carlo events for the largest subsample (94b) are reported in table 8. There the anchoring corrections applied bin-by-bin are also given, together with their errors. Point to point errors are completely described by the correlation matrix in Table 9. Each dataset is fitted in an analogous way and the results are reported in table 10. The full systematic errors are given here, which are partly determined from point-to-point errors (from anchoring and MC statistics) and partly are assigned directly to the slope, as described in Section 7. Table 10 also shows the rescaling factors $\Delta t^*/\Delta t$ for the slope, introduced in relation (9), which are used to combine the results.

Our selection contains a small irreducible physics background from the process $e^+e^- \to \gamma\gamma$. Its cross section within our idealized acceptance is found to be 16.9 pb at 91.1 GeV with a Monte Carlo generator including $\mathrm{O}(\alpha^3)$ terms [22]. The correction to the b^* slope is $-5.5 \times 10^{-5}/\mathrm{GeV}^2$, practically constant with respect to our range of centre-of-mass energies. After this correction the combined value of the effective slope b^* is:

$$b^* = (201 \pm 29 \pm 25) \times 10^{-5}/\mathrm{GeV}^2$$

where the first error is statistical and the second the experimental systematic. The statistical significance of the measurement is $6.8\,\sigma$, which becomes $5.2\,\sigma$ considering the systematic errors.

The result is illustrated by Fig. 12 for the combined data sample. The error bars are statistical only, since many of the systematic errors are correlated in radius and apply directly to the slope. The data are clearly incompatible with the hypothesis of fixed coupling (line $R = 1$). Moreover, the data show a steeper slope than the expected behaviour for vacuum polarization involving only leptons. The fitted linear dependence agrees well with the Standard Model prediction as obtained by BHLUMI, which parameterizes the hadronic contributions according to Burkhardt-Pietrzyk [16]. The newer parameterization [3] by the same authors or the alternative [2] are indistinguishable from [16] in our t range.

The effective slope gives a measurement of the variation of the coupling $\alpha(t)$ from equation (8). By correcting for the small bias of the linear approximation, given in table 4 one gets:

$$\Delta\alpha(-5.96\ \mathrm{GeV}^2) - \Delta\alpha(-1.78\ \mathrm{GeV}^2) = 0.00394 \pm 0.00062 \pm 0.00045$$

Our result is compatible within $1\,\sigma$ with the Standard Model prediction [16], which gives $\delta\,(\Delta\alpha) = 0.00466$ for the same t interval.

If we subtract the precisely known theoretical prediction for the leptonic contribution, $\delta(\Delta\alpha_{lep}) = 0.00202$, from the measured result, we can determine the hadronic contribution as:

$$\Delta\alpha_{had}(-5.96\ \mathrm{GeV}^2) - \Delta\alpha_{had}(-1.78\ \mathrm{GeV}^2) = 0.00193 \pm 0.00062 \pm 0.00045$$

This has a statistical significance of 3.1 σ, reduced to 2.5 σ considering also the systematic errors. This is currently the most significant experimental observation of the running of the QED coupling in a single experiment and also the cleanest when theoretical uncertainties are properly considered.

10 Conclusions

The scale dependence of the effective QED coupling $\alpha(t)$ has been measured from the angular spectrum of small angle Bhabha scattering using the precise OPAL Silicon-Tungsten calorimeters. Despite the narrow accessible t range, the method has high sensitivity due to the high statistics and purity of the data sample. The challenging aspect of the analysis is controlling the residual bias of the reconstructed radial coordinate of Bhabha electrons in the detector to a level below ≈ 10 μm uniformly throughout the acceptance. From a theoretical point of view the environment represents an almost ideal measurement. In fact for this kinematic range the process is almost purely QED, Z interference is very small and the dominant diagram is t-channel single-photon exchange, while s-channel photon exchange is negligible. Small angle Bhabha scattering is one of the most precisely calculable processes. We verified that there is no significant disturbance from photonic radiative corrections in a conservative way and found that the radiative corrections are almost decoupled from the t-slope, at least for the OPAL selection, which strongly reduces non-collinear final states.

We determined the effective slope of the Bhabha momentum transfer distribution which is simply related to the average derivative of $\Delta\alpha$ as a function of t in the range $2\ \mathrm{GeV}^2 \leq -t \leq 6\ \mathrm{GeV}^2$. The observed t-spectrum agrees with the predicted behaviour of the standard Burkhardt-Pietrzyk parameterization within $1\ \sigma$.

This measurement is one of only a very few experimental tests of the running of $\alpha(t)$ in the space-like region, where $\Delta\alpha$ has a smooth behaviour. We obtain the strongest direct evidence for the running of α_{QED} ever achieved in a single experiment, with significance above 5σ. Moreover we report the first clear experimental evidence for the hadronic contribution to the running, with a significance of about 3σ.

Acknowledgements

Usual OPAL Acknowledgements to be added. We are pleased to acknowledge useful discussions with M. Caffo and L. Trentadue.

References

[1] P. J. Mohr and B. N. Taylor, Rev. Mod. Phys. **72** (2000) 351.

[2] S. Eidelman and F. Jegerlehner, Z. Phys. C **67** (1995) 585.

[3] H. Burkhardt and B. Pietrzyk, Phys. Lett. B **513** (2001) 46.

[4] The LEP Collaborations ALEPH, DELPHI, L3 and OPAL, the LEP Electroweak Working Group and the SLD Heavy Flavour Group, CERN-EP-2003-091, hep-ex/0312023.

[5] S. L. Adler, Phys. Rev. D **10** (1974) 3714.

[6] S. Eidelman, F. Jegerlehner, A.L. Kataev, O. Veretin, Phys. Lett. B **454** (1999) 369; F. Jegerlehner, hep-ph/0308117.

[7] TOPAZ Collaboration, I. Levine *et al.*, Phys. Rev. Lett. **78** (1997) 424.

[8] OPAL Collaboration, G. Abbiendi *et al.*, Eur. Phys. J. C **33** (2004) 173

[9] VENUS Collaboration, S. Odaka *et al.*, Phys. Rev. Lett. **81** (1998) 2428.

[10] L3 Collaboration, M. Acciarri *et al.*, Phys. Lett. B **476** (2000) 40

[11] A. B. Arbuzov, D. Haidt, C. Matteuzzi, M. Paganoni and L. Trentadue, Eur. Phys. J. C **34** (2004) 267

[12] OPAL Collaboration, G. Abbiendi *et al.*, Eur. Phys. J. C **14** (2000) 373.

[13] S. Jadach, O. Nicrosini *et al.*, in *Physics at LEP2*, CERN 96-01, ed. G. Altarelli, T. Sjöstrand and F. Zwirner (CERN, Geneva, 1996), Vol. 2, pages 229–298.

[14] A.B. Arbuzov, V.S. Fadin, E.A. Kuraev, L.N. Lipatov, N.P. Merenkov and L. Trentadue, Nucl. Phys. **B485** (1997) 457.

[15] S. Jadach, W. Placzek, E. Richter-Was, B. F. L. Ward and Z. Was, Comput. Phys. Commun. **102** (1997) 229.

[16] H. Burkhardt and B. Pietrzyk, Phys. Lett. B **356** (1995) 398.

[17] OPAL Collaboration, K. Ahmet *et al.*, Nucl. Instrum. Meth. A **305** (1991) 275.

[18] B. F. L. Ward, S. Jadach, M. Melles and S. A. Yost, Phys. Lett. B **450** (1999) 262.

[19] G. Montagna, M. Moretti, O. Nicrosini, A. Pallavicini and F. Piccinini, Phys. Lett. B **459** (1999) 649; Nucl. Phys. B **547** (1999) 39.

[20] S. Jadach, E. Richter-Was, B. F. L. Ward and Z. Was, Comput. Phys. Commun. **70** (1992) 305.

[21] F. A. Berends and R. Kleiss, Nucl. Phys. B **228** (1983) 537.

[22] F. A. Berends and R. Kleiss, Nucl. Phys. B **186** (1981) 22.

Dataset	Right b^* slope $\times 10^{-5}/\mathrm{GeV}^2$	Left b^* slope $\times 10^{-5}/\mathrm{GeV}^2$
93 −2	$139. \pm 100.$	$94. \pm 100.$
93 pk	$211. \pm 100.$	$268. \pm 100.$
93 +2	$153. \pm 102.$	$159. \pm 102.$
94 a	$124. \pm 105.$	$58. \pm 105.$
94 b	$252. \pm 50.$	$217. \pm 50.$
94 c	$16. \pm 184.$	$105. \pm 183.$
95 −2	$247. \pm 100.$	$199. \pm 100.$
95 pk	$251. \pm 123.$	$188. \pm 123.$
95 +2	$47. \pm 100.$	$58. \pm 100.$
Average	$192. \pm 30.$	$171. \pm 30.$
χ^2/d.o.f.	5.9/8	5.1/8

Table 1: Fitted slope for each data subsample and average for the Right and the Left radial distributions. The errors are data and Monte Carlo statistical errors summed in quadrature.

d.o.f. =22	Right side		Left side	
	1993-94	1995	1993-94	1995
(Anchoring correction)	(-12.)	(+19.)	(-9.)	(+18.)
b^* slope ($\times 10^{-5}/\mathrm{GeV}^2$)	$199. \pm 35. \pm 11.$	$173. \pm 61. \pm 13.$	$180. \pm 35. \pm 13.$	$144. \pm 61. \pm 18.$
χ^2_{unc}	45.7	21.4	107.4	32.1
χ^2_{cor} (stat. errors)	35.9	33.8	117.1	45.9
χ^2_{cor} (stat.+syst. errors)	14.7	18.9	38.6	22.0

Table 2: Results of the combined fits to the two homogeneous data sets for the Right and the Left radial distribution, giving the anchoring correction for the slope, the corrected slope with statistical and (anchoring) systematic error and the fit χ^2 for the uncorrected and the corrected distributions with only statistical or statistical plus systematic errors and their covariance matrix.

Radial range	Right b^* slope ($\times 10^{-5}/\mathrm{GeV}^2$)			Left b^* slope ($\times 10^{-5}/\mathrm{GeV}^2$)		
	1993-94	1995	All	1993-94	1995	All
CLEAN	$195. \pm 40.$	$202. \pm 70.$	$196. \pm 35.$	$168. \pm 40.$	$149. \pm 70.$	$163. \pm 35.$
OBSCURED	$207. \pm 76.$	$82. \pm 134.$	$177. \pm 66.$	$225. \pm 76.$	$124. \pm 134.$	$200. \pm 66.$

Table 3: Fitted slope separately for the CLEAN and the OBSCURED radial range of acceptance, for homogeneous data sets. Both the Right and the Left side results are given. The errors are statistical only.

Uncertainty	93 -2	93 pk	93 +2	94a	94b	94c	95 -2	95 pk	95 +2
Anchoring									
uncorrelated	3.	3.	3.	3.	3.	3.	8.	8.	8.
correlated	11.	11.	11.	11.	11.	11.	11.	11.	11.
Dead Material									
uncorrelated	0.	0.	0.	0.	0.	0.	25.	25.	25.
correlated	10.	10.	10.	10.	10.	10.	10.	10.	10.
Radial Metrology									
uncorrelated	0.	0.	0.	0.	0.	0.	0.	0.	0.
correlated	3.	3.	3.	3.	3.	3.	3.	3.	3.
Radial Thermal									
uncorrelated	0.	0.	0.	0.	0.	0.	0.	0.	0.
correlated	1.	1.	1.	1.	1.	1.	3.	3.	3.
Background									
uncorrelated	0.	0.	0.	0.	0.	0.	0.	0.	0.
correlated	5.	4.	2.	1.	1.	2.	1.	1.	1.
Energy									
uncorrelated	0.	0.	0.	0.	0.	0.	0.	0.	0.
correlated	8.	8.	8.	8.	8.	8.	8.	8.	8.
Beam parameters									
uncorrelated	5.	9.	6.	2.	2.	4.	4.	7.	9.
correlated	2.	2.	2.	2.	2.	2.	2.	2.	2.
Radial resolution									
uncorrelated	0.	0.	0.	0.	0.	0.	0.	0.	0.
correlated	4.	4.	4.	4.	4.	4.	7.	7.	7.
Acollinearity bias									
uncorrelated	0.	0.	0.	0.	0.	0.	0.	0.	0.
correlated	3.	3.	3.	3.	3.	3.	3.	3.	3.
M.C. statistics									
uncorrelated	21.	21.	21.	38.	21.	65.	21.	21.	21.
correlated	0.	0.	0.	0.	0.	0.	0.	0.	0.
Linear approx. bias									
uncorrelated	0.	0.	0.	0.	0.	0.	0.	0.	0.
correlated	8.	12.	16.	12.	12.	12.	8.	12.	16.
Sum									
uncorrelated	22.	23.	22.	38.	21.	66.	34.	35.	35.
correlated	20.	22.	24.	22.	21.	22.	21.	23.	25.
Total Systematic error	29.	32.	33.	44.	30.	69.	40.	41.	43.

Table 4: Summary of the experimental systematic uncertainties on the measurement of the effective slope b^* for the nine data sets on the Right side. They are broken down into the components correlated and uncorrelated among the data sets. All errors are in units of $10^{-5}/\mathrm{GeV}^2$.

Sample	93 -2	93 pk	93 +2	94 a	94 b	94 c	95 -2	95 pk	95 +2
93 -2	1.00	0.04	0.04	0.04	0.07	0.02	0.04	0.03	0.04
93 pk	0.04	1.00	0.05	0.04	0.08	0.02	0.04	0.04	0.05
93 +2	0.04	0.05	1.00	0.05	0.09	0.03	0.04	0.04	0.05
94 a	0.04	0.04	0.05	1.00	0.08	0.02	0.04	0.03	0.04
94 b	0.07	0.08	0.09	0.08	1.00	0.04	0.07	0.07	0.09
94 c	0.02	0.02	0.03	0.02	0.04	1.00	0.02	0.02	0.03
95 -2	0.04	0.04	0.04	0.04	0.07	0.02	1.00	0.08	0.10
95 pk	0.03	0.04	0.04	0.03	0.07	0.02	0.08	1.00	0.09
95 +2	0.04	0.05	0.05	0.04	0.09	0.03	0.10	0.09	1.00

Table 5: The experimental correlation matrix for the nine data sets.

Error source	$\delta b \times 10^{-5}/GeV^2$		
	peak	peak - 2	peak + 2
Photonic corrections	14.	14.	14.
Z-interference	7.	16.	14.
Total	16.	21.	20.

Table 6: The estimated theoretical uncertainties on the measurement of the effective slope b^*, at centre-of-mass energies of 91.1, 89.1, 93.1 GeV.

Bin	R_{in}	R_{out}	$-t_{in}$	$-t_{out}$	$< -t >$
	(cm)		(GeV^2)		
1	7.2584	8.2665	1.80	2.34	2.05
2	8.2665	9.2746	2.34	2.95	2.62
3	9.2746	10.7868	2.95	3.98	3.41
4	10.7868	11.7949	3.98	4.76	4.35
5	11.7949	13.3071	4.76	6.06	5.36

Table 7: Bin definitions for the radial distribution. The corresponding $-t$ and $< -t >$ values are determined assuming a reference energy $\sqrt{s} = 91.1$ GeV.

Bin	N_{data}	N_{MC}	Ratio $R = N_{data}/N_{MC}$				
			anchoring correction	*corrected value*	*stat.err.* (*data*)	*syst.err.* (*MCstat.*)	*syst.err.* (*anchoring*)
1	1310496	1313450	-0.00019	0.99756	0.00087	0.00040	0.00045
2	927931	931473	+0.00082	0.99701	0.00103	0.00047	0.00052
3	941500	938667	-0.00181	1.00121	0.00103	0.00047	0.00040
4	431654	430794	+0.00116	1.00316	0.00153	0.00068	0.00064
5	458295	455492	-0.00032	1.00583	0.00149	0.00067	0.00039

Table 8: Detailed fit inputs for the largest data subsample (94b). Each row corresponds to a radial bin and gives: number of data and MC events normalized to the data sample; their ratio and the applied anchoring correction; errors attributed to the points: data and MC statistical error and systematic error of the anchoring procedure.

Bin	1	2	3	4	5
1	1.00	-0.08	0.01	0.01	0.01
2	-0.08	1.00	-0.05	0.01	0.00
3	0.01	-0.05	1.00	-0.05	0.00
4	0.01	0.01	-0.05	1.00	-0.03
5	0.01	0.00	0.00	-0.03	1.00

Table 9: Error correlation matrix for the 94b radial distribution given in the previous table.

Dataset	$\sqrt{s}$ (GeV)	$\Delta t^*/\Delta t$	b^* slope $\times 10^{-5}/\mathrm{GeV}^2$
93 -2	89.4510	1.021	$132. \pm 100. \pm 29.$
93 pk	91.2228	0.981	$179. \pm 99. \pm 32.$
93 $+2$	93.0362	0.943	$163. \pm 102. \pm 33.$
94 a	91.2354	0.981	$140. \pm 100. \pm 44.$
94 b	91.2170	0.981	$275. \pm 47. \pm 30.$
94 c	91.2436	0.981	$-18. \pm 175. \pm 69.$
95 -2	89.4416	1.021	$271. \pm 100. \pm 40.$
95 pk	91.2860	0.980	$277. \pm 123. \pm 41.$
95 $+2$	92.9720	0.945	$80. \pm 100. \pm 43.$
Average			$207. \pm 29. \pm 25.$
χ^2/d.o.f.			7.4/8 6.6/8

Table 10: Fitted b^* slope for each data subsample and average, for the radial distribution specified in tables 7 and 8. The average centre-of-mass energy of each subsample is also reported, together with the factor $\Delta t^*/\Delta t$ which rescales the fitted slope to the reference energy value $\sqrt{s} = 91.1$ GeV. The first error is statistical, the second is the full systematic. Error correlations are given in table 5.

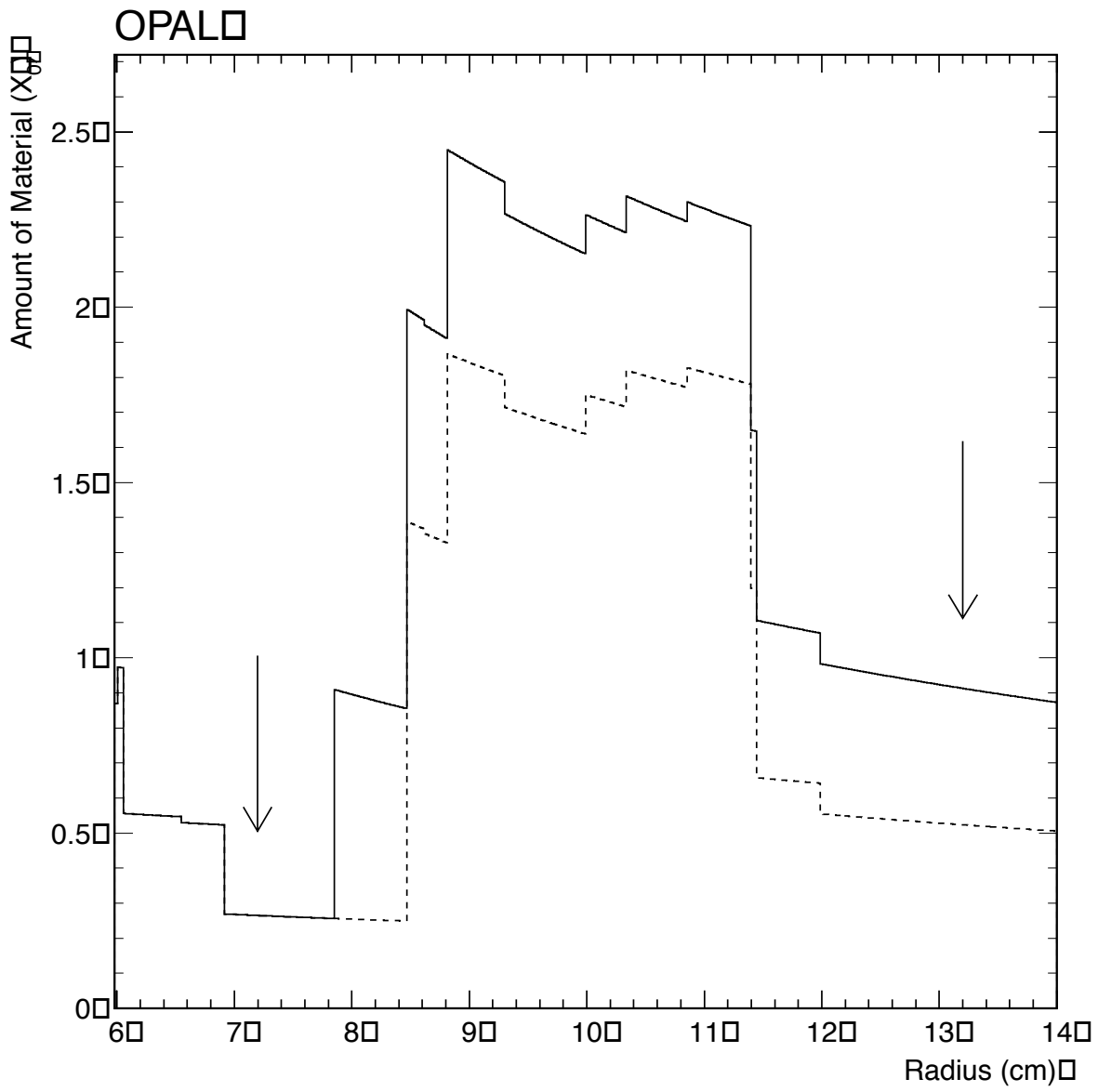

Figure 1: The calculated material traversed by particles originating at the interaction point as a function of calorimeter radius for the 1993–94 detector configuration. The solid curve corresponds to the left, the dotted curve to the right side. The larger amount of material on the left is due to the passage of cables from the OPAL microvertex detector. The arrows show the location of the acceptance definition cuts on shower radius.

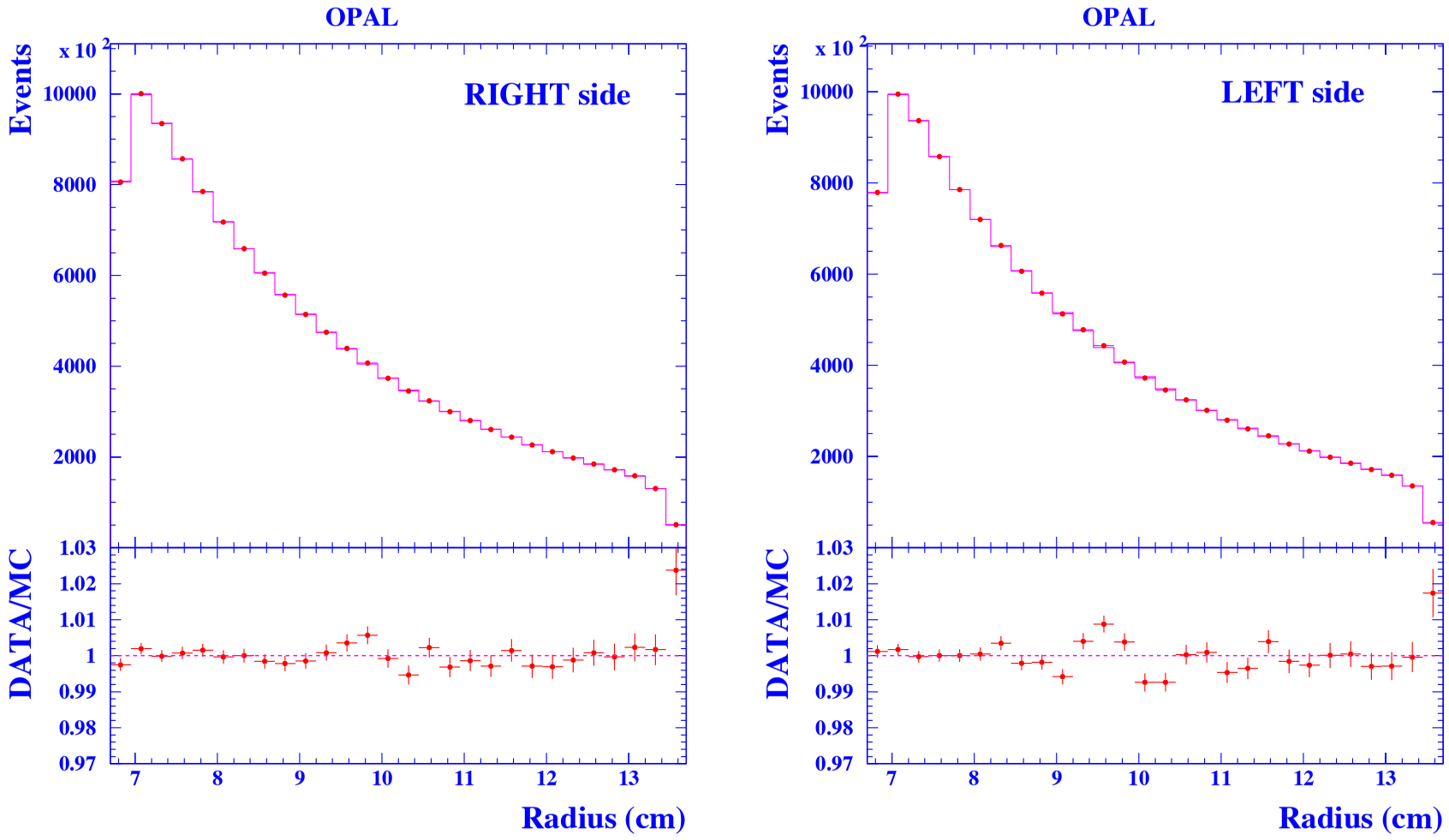

Figure 2: Radial distributions after the isolation cuts for the complete LEP1 statistics in the Right and Left calorimeters. The points show the data and the histogram the Monte Carlo prediction normalized to the same number of events. The lower plots show the ratio between data and Monte Carlo.

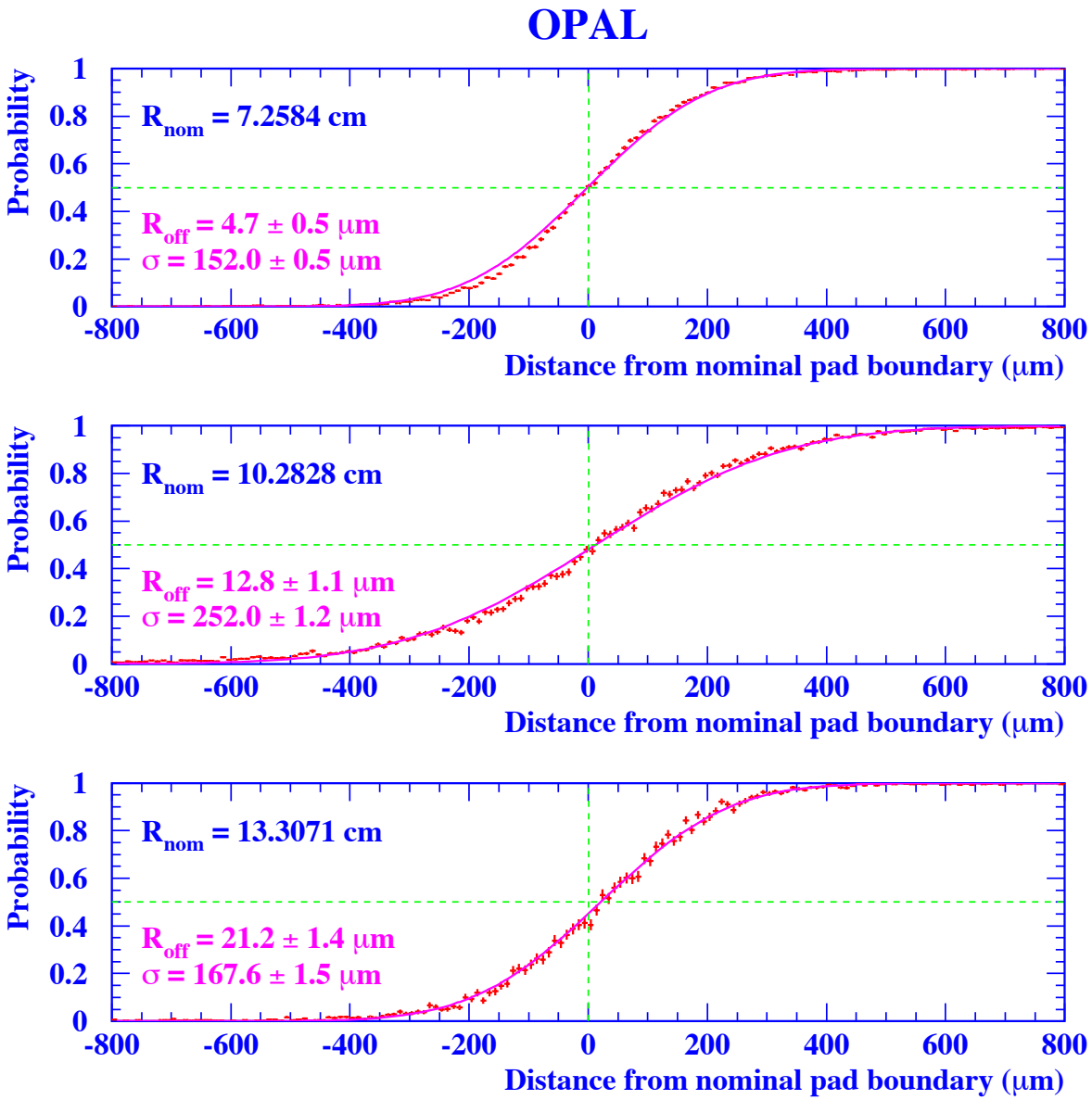

Figure 3: Pad boundary images obtained for the Si layer at 4 X_0 at three different radial positions corresponding to the inner edge, the middle portion and the outer edge of the acceptance. The solid curve shows the fitted function, whose parameters R_{off} and σ_a are given.

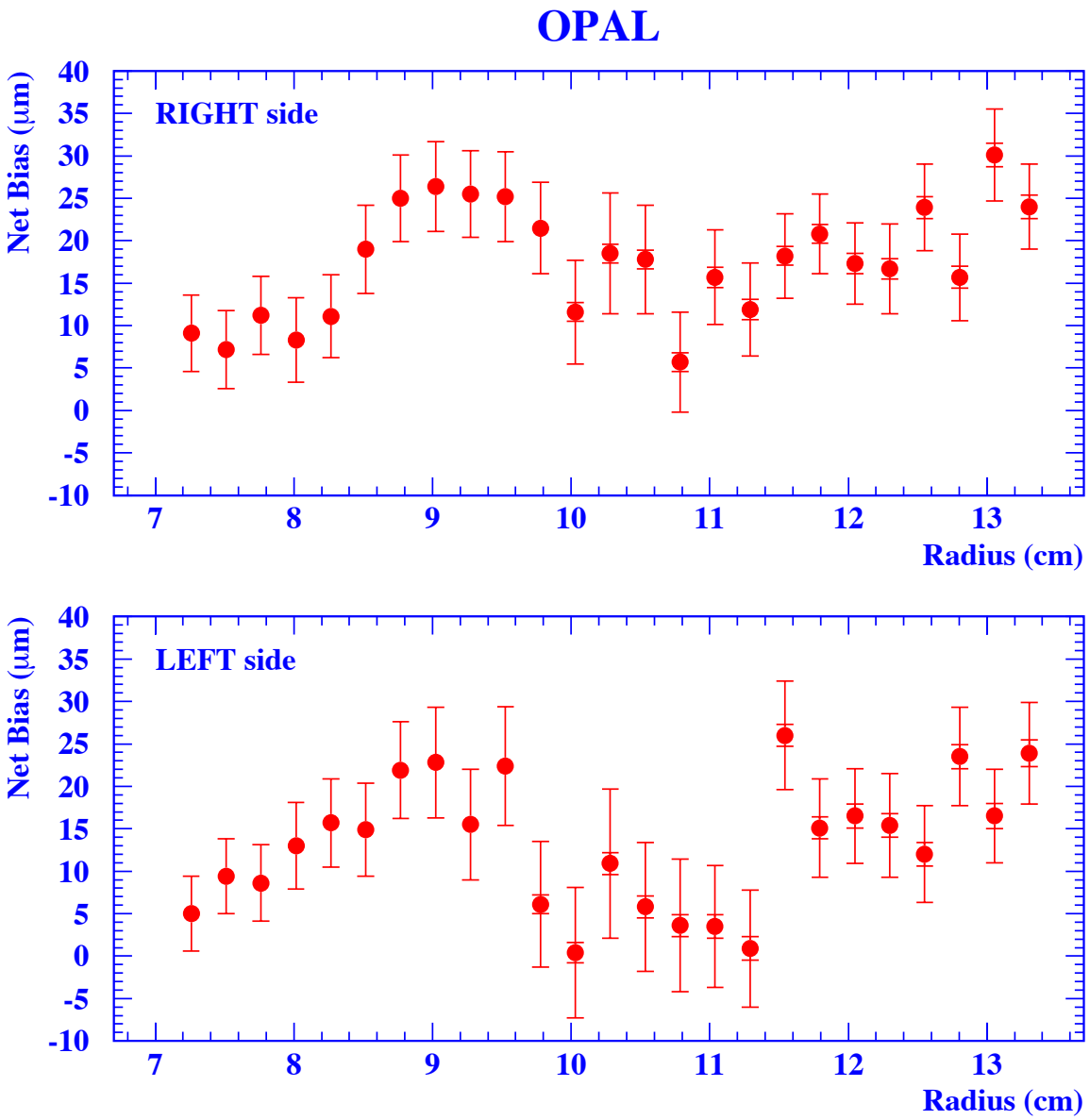

Figure 4: The total net bias (*anchor*) as a function of radius for the Right and the Left radial coordinate determined for the Si layer at 4 X_0, for the combined 1993-94 data sample. The full error bars show the total error, the inner bars the statistical component.

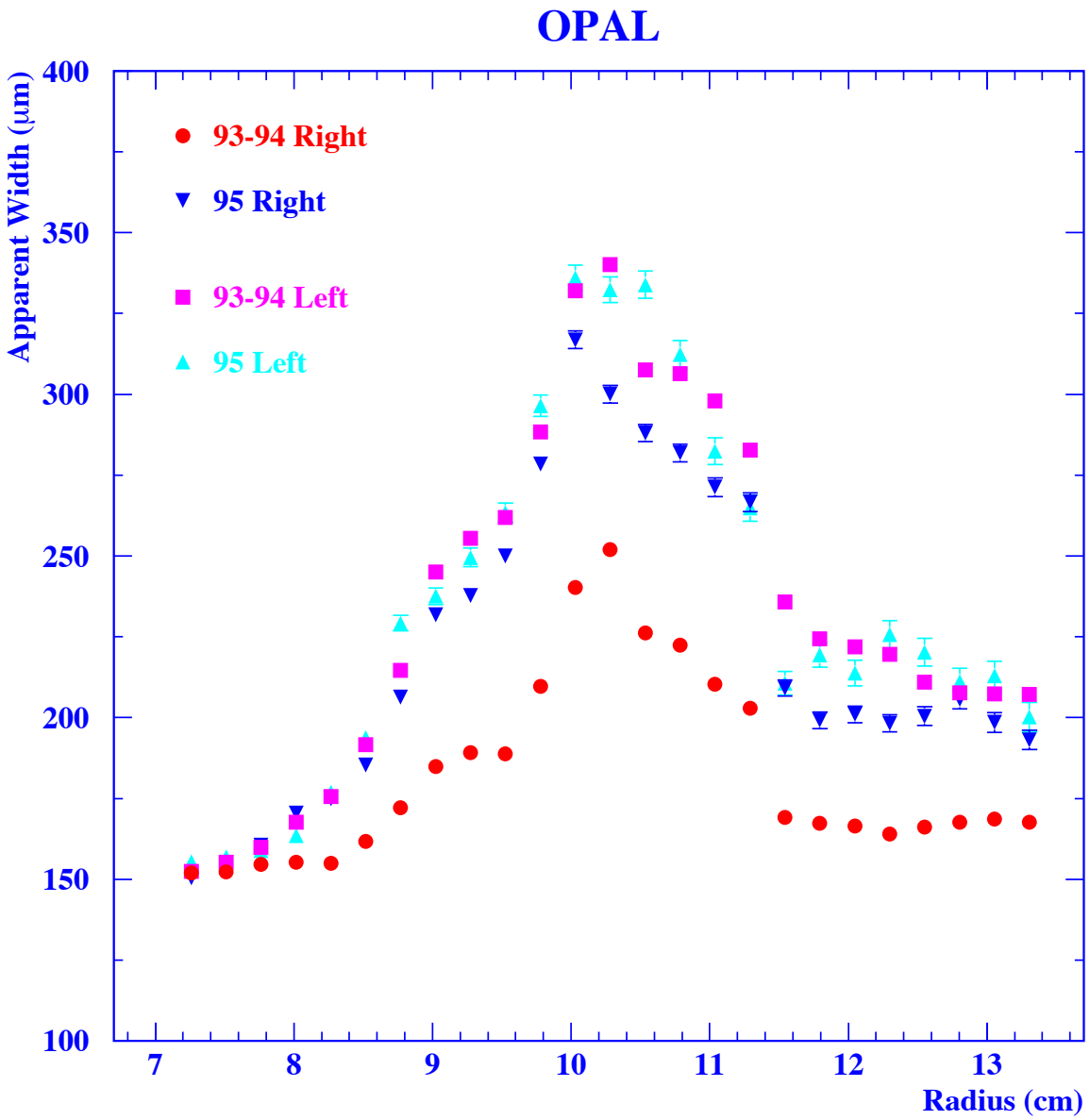

Figure 5: The apparent width σ_a as a function of radius determined from the anchoring procedure for the Si Layer at 4 X_0 for the four homogeneous data subsamples. The errors are statistical only.

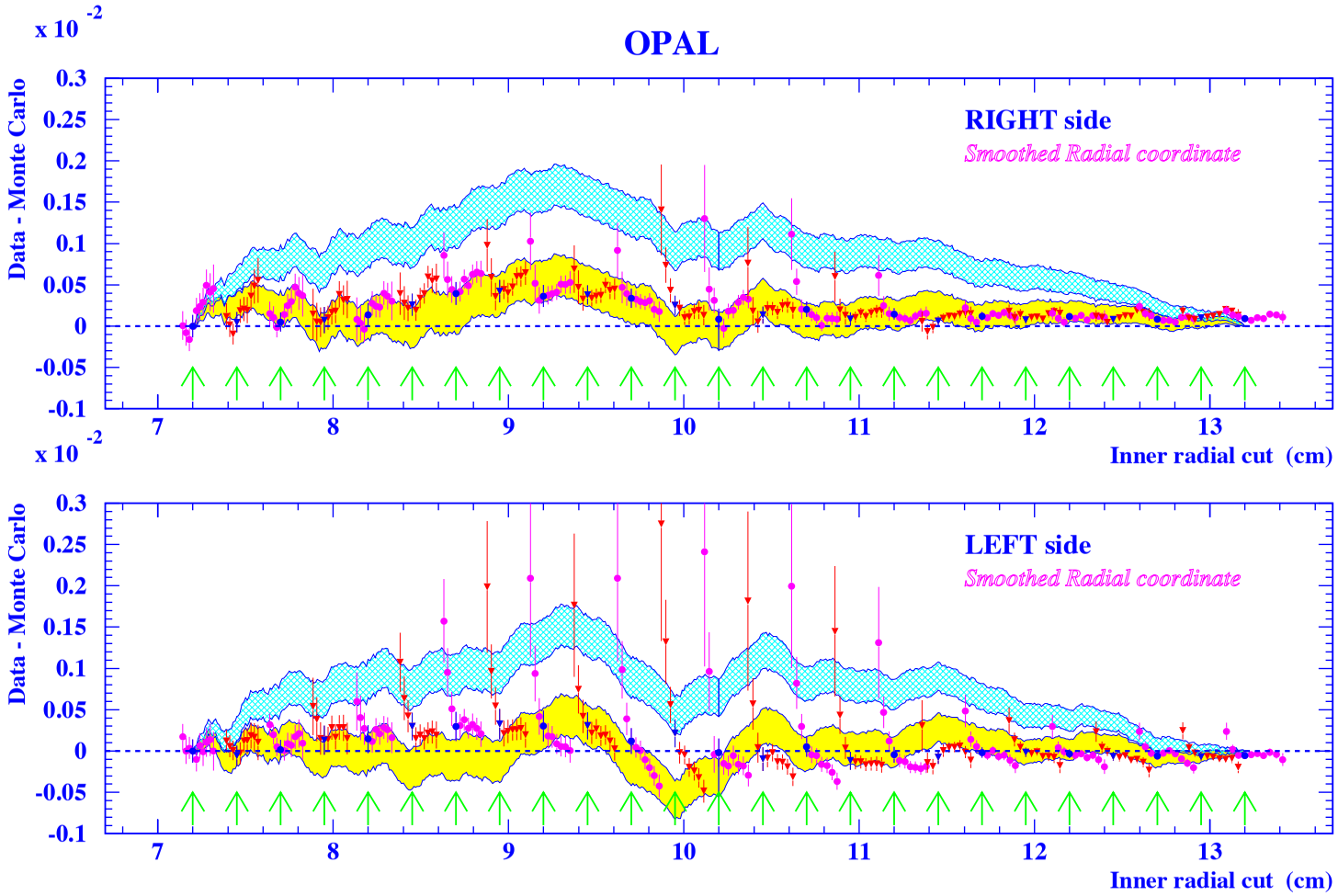

Figure 6: Study of the final reconstructed radial coordinate. *(rgk: The "smoothed radial coordinate" text should be removed from the fig.)* The shaded band shows the relative change in acceptance between data and Monte Carlo as a function of the definition cut on the inner radius for the combined 1993-94 data sample. The width of the band shows the (highly correlated) statistical errors. The solid points correspond to the coordinate bias measured by the anchoring procedure in Si-layers from 1 X_0 to 10 X_0, with the total errors shown. Triangles and circles designate even and odd rings of radial pads respectively. Here the anchor at $R = 7.2$ cm is fixed to lie at zero. The arrows show the location of the radial pad boundaries in layer 7 X_0. The hatched band shows the prediction for zero running ($\alpha(t) \equiv \alpha_0$).

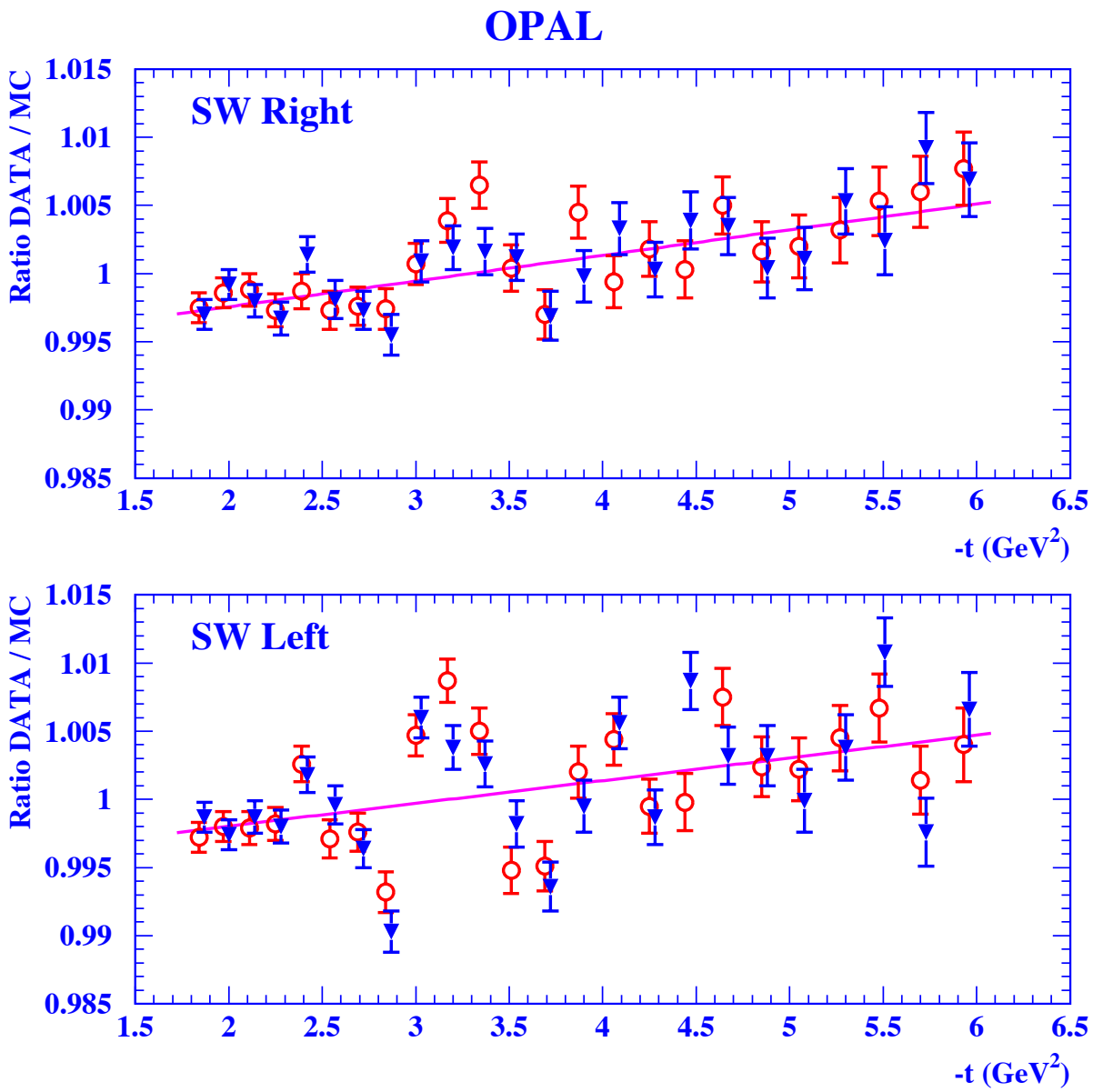

Figure 7: Ratio of data and Monte Carlo (with $\Delta\alpha$ set to zero) for the combination of all LEP1 data, for the Right and Left sides. Each point corresponds to a bin of one radial pad. The solid triangles show the data corrected with anchors in layer 4 X_0, the empty circles the uncorrected data (slightly shifted for clarity), with statistical errors in both cases. The line shows the fit result.

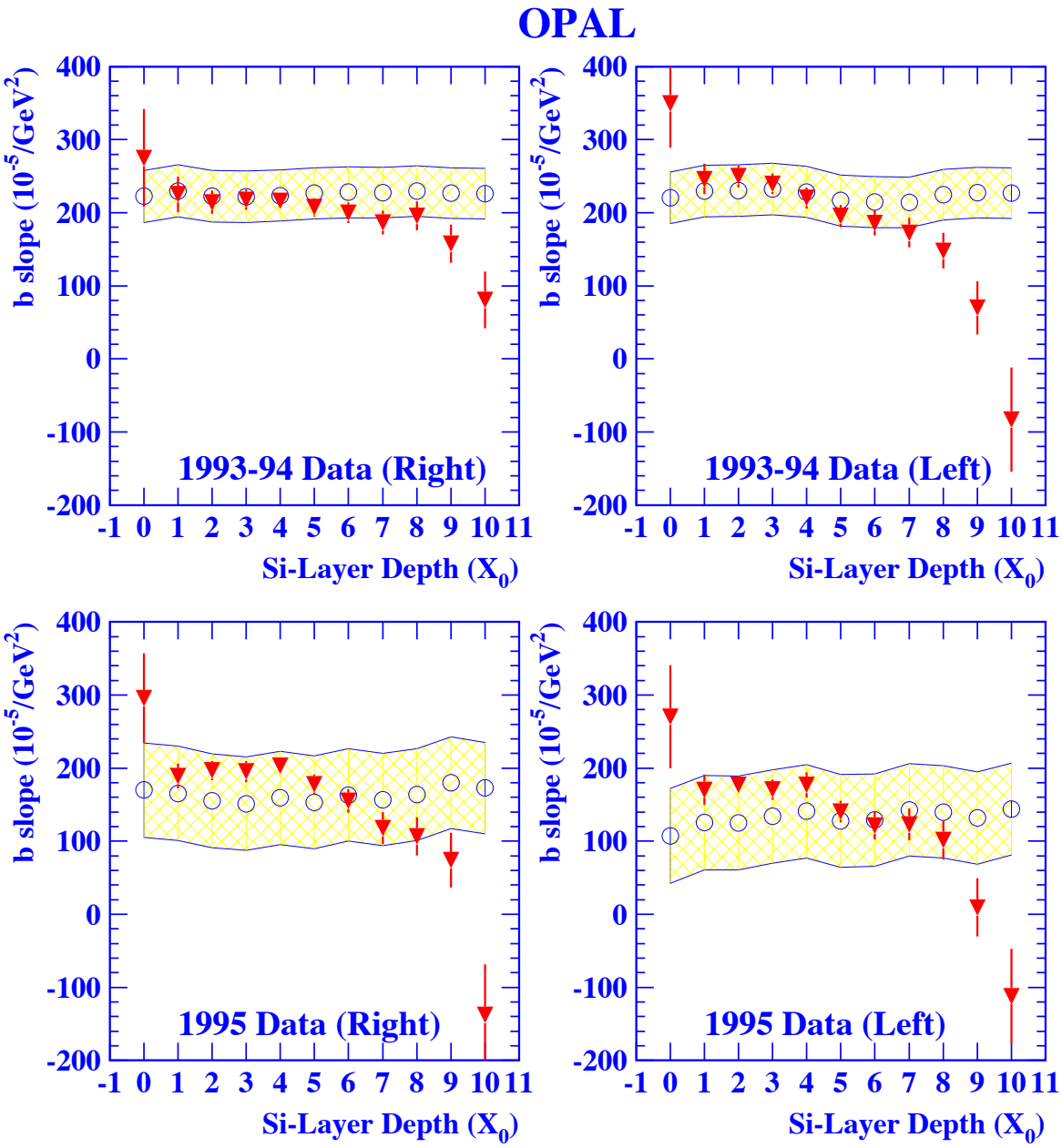

Figure 8: Fitted slope as a function of the anchoring layer for homogeneous data combinations. The open circles show results obtained from uncorrected radial distributions, with the hatched band representing the (correlated) statistical error. The solid triangles show results from distributions corrected by anchoring, with the error bars representing only the systematic errors.

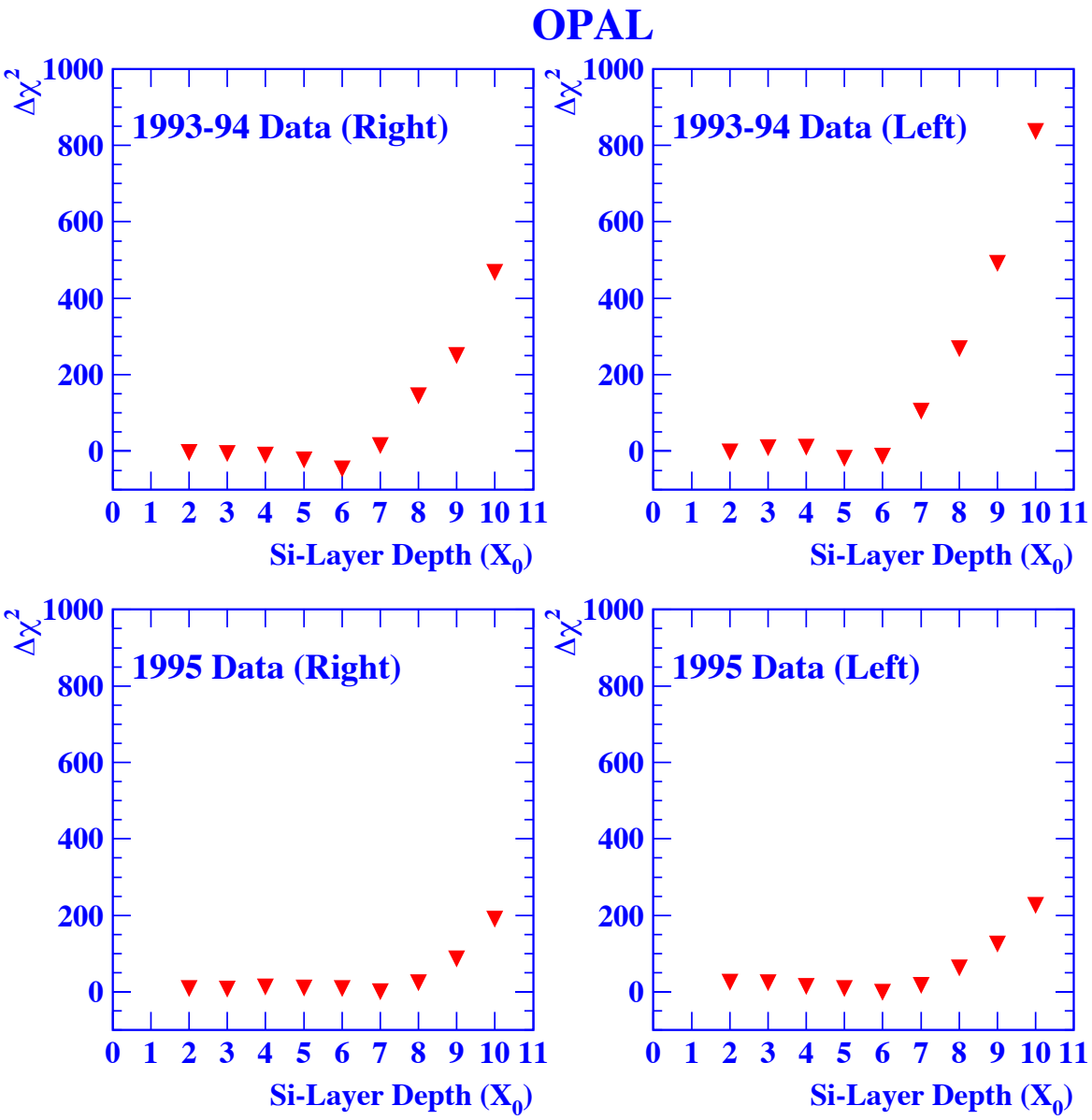

Figure 9: Difference between corrected and uncorrected χ^2 (d.o.f.=22) as a function of the anchoring layer for the homogeneous data sets. Only statistical errors are considered.

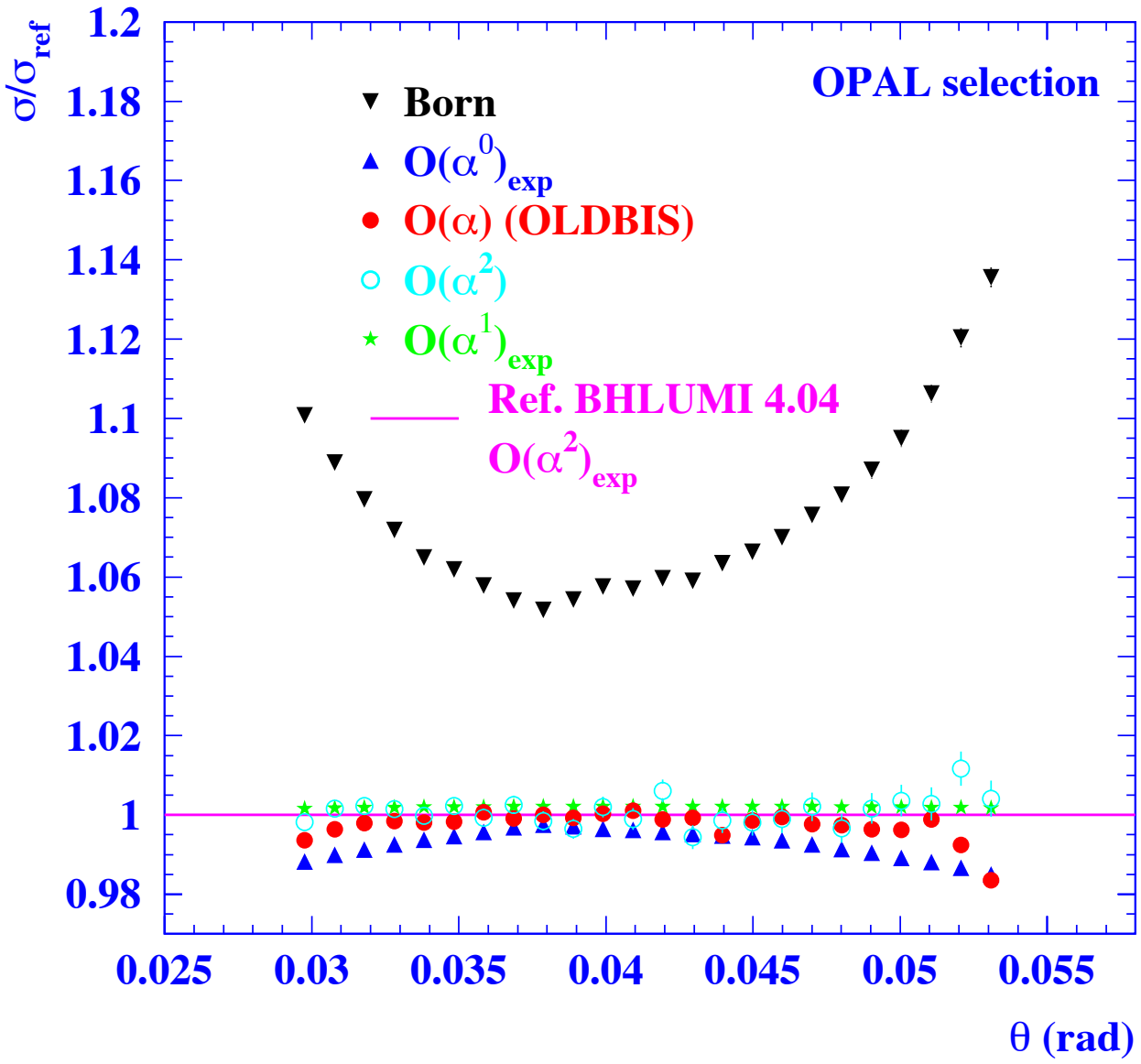

Figure 10: Differential cross section as a function of the polar scattering angle calculated by the BHLUMI package for the OPAL selection in different perturbative approximations, normalized to the reference BHLUMI calculation. Vacuum polarization, Z-interference and s-channel photon contributions are switched off.

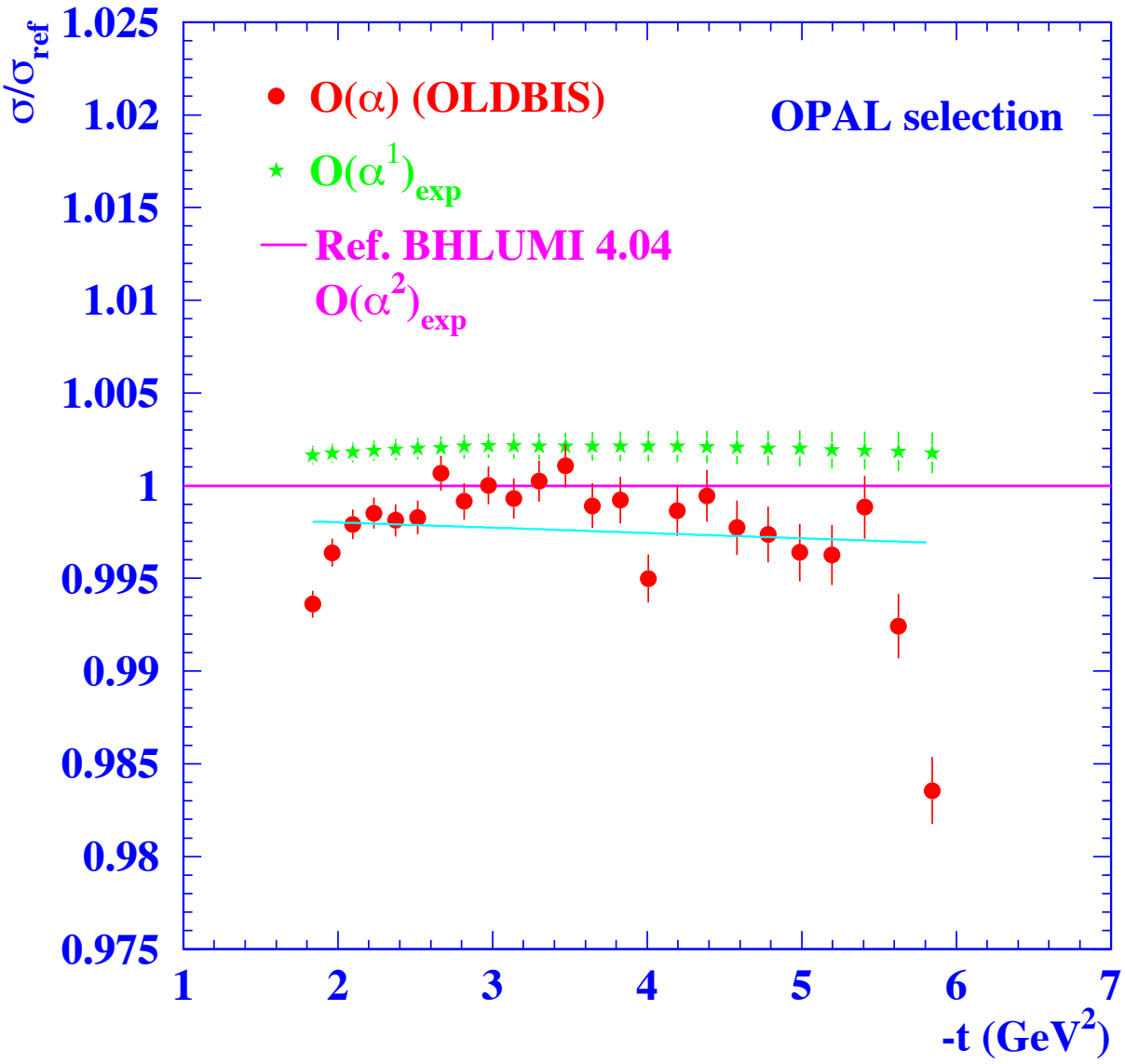

Figure 11: Differential cross section as a function of the polar scattering angle calculated by the BHLUMI package for the OPAL selection with exact (OLDBIS) or exponentiated $\mathcal{O}(\alpha)$ matrix element, normalized to the reference BHLUMI calculation. Vacuum polarization, Z-interference and s-channel photon contributions are switched off. The fitted line is used to conservatively assess the theoretical uncertainty.

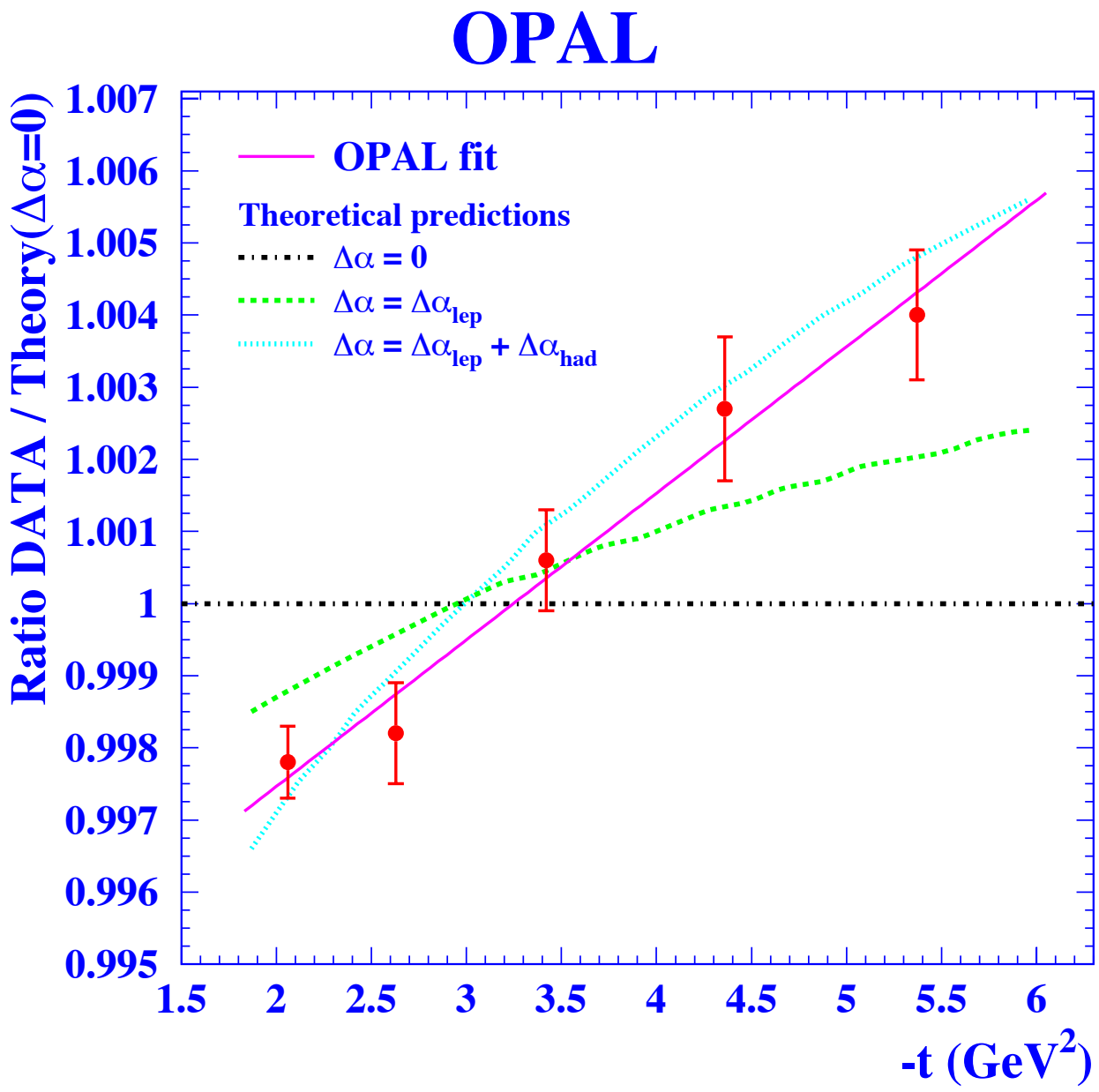

Figure 12: $|t|$ spectrum normalized to the BHLUMI theoretical prediction for a fixed coupling ($\Delta\alpha = 0$). The points show the combined LEP1 data with statistical error bars, the solid line is our fit. The horizontal dot-dashed axis would be the prediction if α were fixed. The dashed curve is the prediction of running α determined by vacuum polarization with only virtual lepton pairs ($\Delta\alpha = \Delta\alpha_{lep}$), the dotted curve with both lepton and quark pairs, calculated by the Burkhardt-Pietrzyk parameterization.